RESEARCH ARTICLE SUMMARY

SYSTEMS BIOLOGY

A protein interaction landscape of breast cancer

Minkyu Kim, Jisoo Park, Mehdi Bouhaddou, Kyumin Kim, Ajda Rojc, Maya Modak, Margaret Soucheray, Michael J. McGregor, Patrick O'Leary, Denise Wolf, Erica Stevenson, Tzeh Keong Foo, Dominique Mitchell, Kari A. Herrington, Denise P. Muñoz, Beril Tutuncuoglu, Kuei-Ho Chen, Fan Zheng, Jason F. Kreisberg, Morgan E. Diolaiti, John D. Gordan, Jean-Philippe Coppé, Danielle L. Swaney, Bing Xia, Laura van 't Veer, Alan Ashworth, Trey Ideker*, Nevan J. Krogan*

INTRODUCTION: Advances in DNA sequencing technology have enabled the widespread analysis of breast tumor genomes, creating a catalog of genetic mutations that may initiate or drive tumor progression. In addition to common mutations in well-known cancer genes, such as *TP53* and *PIK3CA*, breast cancers harbor a variety of rare mutations with low prevalence across the patient population. Despite this heterogeneity, the majority of breast cancer patients are treated using broad chemotherapy or hormone therapies, which vary widely in effectiveness across patients. Therefore, there is an urgent need to develop targeted therapies matched to the specific molecular alterations in each patient's tumor, with the goal of improving efficacy, reducing toxicity, and avoiding unnecessary treatment.

RATIONALE: A key question is how these rare alterations elicit pathologic consequences, control patient outcomes, and, ultimately, translate into personalized therapies. An answer lies in understanding how individual gene mutations converge on multigene functional modules, including the signaling pathways that orchestrate cell proliferation, apoptosis, and DNA repair. To broadly enable a pathway-based understanding of cancer, we must first generate comprehensive maps of cancer molecular networks in relevant malignant and premalignant cellular contexts.

RESULTS: To this end, we used affinity purification combined with mass spectrometry (AP-MS) to catalog protein-protein interactions (PPIs) for 40 proteins significantly altered in breast cancer, including multidimensional measurements across mutant and normal protein isoforms and across cancerous and noncancerous cellular contexts. Approximately 79% of the PPIs that we identified have not been previously reported, and 81% are not shared across cell lines, which illustrates a substantial rewiring of PPIs driven by different cellular contexts. Notably, interacting proteins specific to two breast cancer cell lines (MCF7 and MDA-MB-231) are more frequently mutated in breast tumors than interacting proteins recovered in nontumorigenic MCF10A cells, which implies that proteins interacting with known cancer drivers may also contribute to the onset of cancer.

AP-MS analysis of PIK3CA identified previously unidentified interacting proteins (BPIFA1 and SCGB2A1) that act as potent negative regulators of the PI3K-AKT pathway in multiple breast cancer cell contexts, providing new mechanistic and therapeutic insights into the regulation of this key signaling pathway. Furthermore, UBE2N emerged as a functionally relevant interactor of BRCA1, and we show that its expression could serve as a potential biomarker of response to poly(ADP-ribose) polymerase (PARP) inhibitors and other DNA repair targeted therapies. We also found that the protein phosphatase 1 (PP1) regulatory subunit spinophilin interacts with and regulates dephosphorylation of BRCA1 and other DNA repair proteins to promote DNA double-strand break repair.
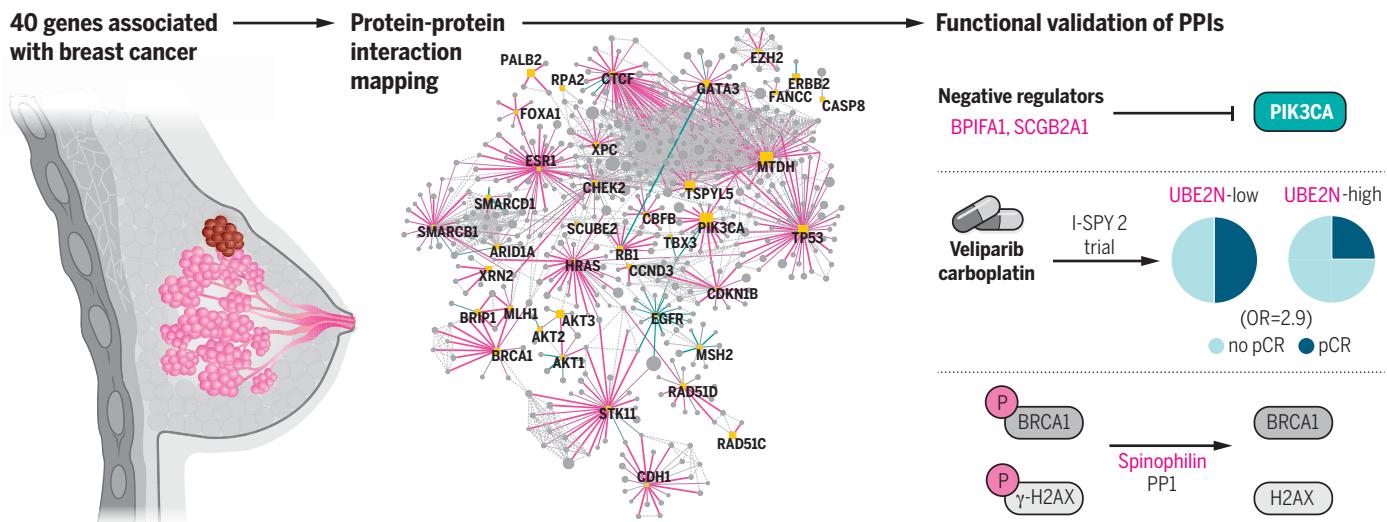
CONCLUSION: Our study demonstrates that systematic PPI maps provide a useful resource in contextualizing uncharacterized mutations within signaling pathways and protein complexes. Such maps effectively identify previously unidentified cancer susceptibility genes and druggable vulnerabilities in not only breast cancer but head and neck cancer as well (Swaney *et al.*, this issue). These efforts are informing hierarchical maps of protein complexes and systems in both healthy and diseased cells (Zheng *et al.*, this issue), which can be used to stratify patients for known anticancer therapies and drive the discovery of therapeutic targets for cancer as well as a variety of other diseases. ∎

READ THE FULL ARTICLE AT
https://doi.org/10.1126/science.abf3066

Breast cancer interactome study. Large-scale protein interaction maps using breast cancer genes provide a framework for mechanistically interpreting cancer genomic data and can identify valuable previously unidentified therapeutic targets. OR, odds ratio; pCR, pathologic complete response.

RESEARCH ARTICLE

SYSTEMS BIOLOGY

A protein interaction landscape of breast cancer

Minkyu Kim[1,2,3,4], Jisoo Park[4,5], Mehdi Bouhaddou[1,2,3,4], Kyumin Kim[1,2,3,4]†, Ajda Rojc[1,2,3,4], Maya Modak[1,2,3,4], Margaret Soucheray[1,2,3,4], Michael J. McGregor[1,2,3,4], Patrick O'Leary[4,6], Denise Wolf[4,6], Erica Stevenson[1,2,3,4], Tzeh Keong Foo[7], Dominique Mitchell[3,6,8], Kari A. Herrington[9], Denise P. Muñoz[4,6], Beril Tutuncuoglu[1,2,3,4], Kuei-Ho Chen[1,2,3,4], Fan Zheng[4,5], Jason F. Kreisberg[4,5], Morgan E. Diolaiti[4,6], John D. Gordan[3,6,8], Jean-Philippe Coppé[4,6], Danielle L. Swaney[1,2,3,4], Bing Xia[7], Laura van 't Veer[4,6], Alan Ashworth[4,6], Trey Ideker[4,5,10]*, Nevan J. Krogan[1,2,3,4]*

Cancers have been associated with a diverse array of genomic alterations. To help mechanistically understand such alterations in breast-invasive carcinoma, we applied affinity purification–mass spectrometry to delineate comprehensive biophysical interaction networks for 40 frequently altered breast cancer (BC) proteins, with and without relevant mutations, across three human breast cell lines. These networks identify cancer-specific protein-protein interactions (PPIs), interconnected and enriched for common and rare cancer mutations, that are substantially rewired by the introduction of key BC mutations. Our analysis identified BPIFA1 and SCGB2A1 as PIK3CA-interacting proteins, which repress PI3K-AKT signaling, and uncovered USP28 and UBE2N as functionally relevant interactors of BRCA1. We also show that the protein phosphatase 1 regulatory subunit spinophilin interacts with and regulates dephosphorylation of BRCA1 to promote DNA double-strand break repair. Thus, PPI landscapes provide a powerful framework for mechanistically interpreting disease genomic data and can identify valuable therapeutic targets.

B reast cancer (BC) is the most common malignancy in women and the second leading cause of cancer-related death in the United States, where an estimated 281,550 women and 2650 men will be newly diagnosed in 2021 (*1*). The disease has been divided into different subtypes, largely on the basis of the presence or absence of three key proteins: estrogen receptor (ER), progesterone receptor (PR), and human epidermal growth factor receptor 2 (HER2/ERBB2). Despite this and much additional heterogeneity at the molecular level, the majority of BC patients are treated using untailored chemotherapy or hormone therapies. Therefore, there is an urgent need to develop targeted therapies matched to the specific molecular alterations in a tumor, with the goal of achieving better efficacy and avoiding unnecessary treatment.

Advances in DNA sequencing technology have enabled the widespread analysis of breast tumor genomes, creating a catalog of genetic mutations that may initiate or drive tumor progression (*2*, *3*). In addition to common mutations in well-known cancer genes, such as *TP53* and *PIK3CA*, BCs harbor many additional mutations, each of which is rarely seen across the patient population. A key question is how these less-common alterations, dispersed across a multitude of genes, elicit pathologic consequences and patient outcomes. An answer may lie in understanding how individual gene mutations converge on multigene functional modules, including the signaling pathways that orchestrate cell proliferation and apoptosis and the DNA repair complexes (*4–15*). To broadly enable a pathway-based understanding of cancer, we must first generate general and comprehensive maps of cancer molecular networks in relevant malignant and premalignant cell contexts.

Protein-protein interaction mapping of BC drivers

Using The Cancer Genome Atlas (TCGA) analysis of BC tumors (*2*, *3*), we collected a panel of genes that are associated with molecular alterations, in terms of cell growth, proliferation, and genome stability in BC, and used this list to guide the selection of 40 proteins for the generation of protein-protein interaction (PPI) networks. Our selected targets included proteins with well-known roles in BC (e.g., TP53, PIK3CA, CDH1, and BRCA1) as well as less–well-characterized proteins with recurrent mutations (e.g., CHEK2, MLH1, SMARCB1, and XPC) (*16–19*). Notably, 93% of BC tumors included in the TCGA analysis harbor an al-

teration in one or more of these 40 genes (Fig. 1A). Three breast cell lines derived from human mammary epithelium—MCF7 (ER+, luminal A subtype), MDA-MB-231 [ER–, PR–, HER2– triple-negative (TN) subtype], and MCF10A (nontumorigenic mammary epithelial cells)—were selected for the PPI analysis because they have been shown to replicate therapeutically relevant responses found in BC tumors (*20*), their RNA profiles are highly correlated with those of BC tumors (*21*), and ER+ and TN subtypes together account for ~90% of BC patients (*22*). We reasoned that comparing protein networks among ER+, TN, and nontumorigenic models would allow us to study how PPI networks are altered between normal and tumorigenic backgrounds as well as how they are influenced by different mammary epithelial lineages.

To generate PPI maps, "bait" proteins were cloned into triple FLAG-tagged lentiviral vectors (table S2), individually transduced into each cell line, and expressed in biological triplicate through a doxycycline inducible promoter (Fig. 1B). Cells were harvested after ~40 hours of doxycycline induction, and anti-FLAG tag–based affinity purification (AP) was performed followed by mass spectrometry (MS) to detect interacting "prey" proteins in an unbiased manner. We used two PPI scoring algorithms to quantify high-confidence interacting proteins: compPASS (*23*, *24*) and SAINTexpress (*25*) (Materials and methods). Although overexpression of tagged baits may generate possible artifacts, it permits the capture of PPIs in a highly sensitive and reproducible manner with a relatively uniform background signal, which can be removed by the appropriate algorithms. We and many others have used overexpression affinity purification–mass spectrometry (AP-MS) to characterize thousands of physiologically relevant PPIs (*26–30*). Using this approach, we identified a total of 589 high-confidence PPIs involving 493 prey proteins (Fig. 1C; fig. S1, A and B; and tables S3 and S4). Collectively, 78% of the BC PPIs we identified were not previously reported in PPI databases (CORUM, BioPlex 2.0, IMEx, and the low-throughput and multivalidated BIOGRID) (Fig. 1C). The high percentage of new interactions may reflect cell type–enriched PPIs because nearly all systematic PPI analyses to date have been performed in HEK293T or HeLa cell lines (*24*, *26*, *27*, *31*, *32*).

PPIs often suggest functional relationships among proteins that work together to regulate a specific cellular process. Previously, we and others have found a significant enrichment of frequently mutated proteins in large PPI repositories (*8–12*, *33–35*). Similarly, we investigated whether our BC PPI network showed enrichment for three major types of alterations—nonsynonymous mutations, chromosomal copy number variations (CNVs), and mRNA expression

¹Department of Cellular and Molecular Pharmacology, University of California, San Francisco, CA, USA. ²The J. David Gladstone Institute of Data Science and Biotechnology, San Francisco, CA, USA. ³Quantitative Biosciences Institute, University of California, San Francisco, CA, USA. ⁴The Cancer Cell Map Initiative, San Francisco and La Jolla, CA, USA. ⁵Department of Medicine, University of California, San Diego, CA, USA. ⁶Department of Medicine, Helen Diller Family Comprehensive Cancer Center, University of California, San Francisco, CA, USA. ⁷Department of Radiation Oncology, Rutgers Cancer Institute of New Jersey, New Brunswick, NJ, USA. ⁸Division of Hematology/Oncology, University of California, San Francisco, CA, USA. ⁹Department of Biochemistry and Biophysics, Center for Advanced Light Microscopy, University of California, San Francisco, CA, USA. ¹⁰Department of Bioengineering, University of California, San Diego, CA, USA.
*Corresponding author. Email: nevan.krogan@ucsf.edu (N.J.K.); tideker@ucsd.edu (T.I.)
†Present address: Molecular and Computational Biology Program, University of Southern California, Los Angeles, CA, USA.
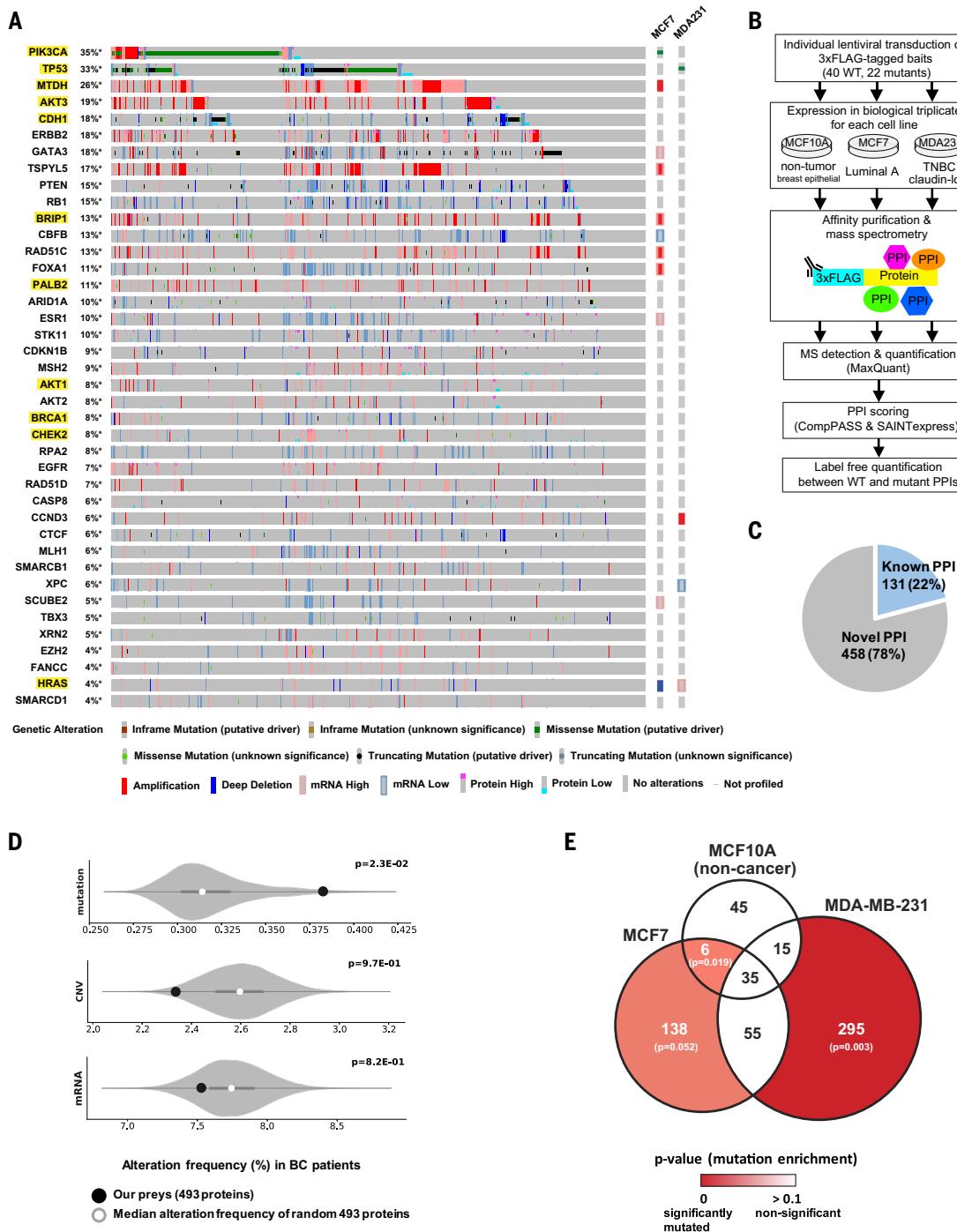
Fig. 1. Overview of PPI mapping in breast epithelial cells. (**A**) The gene alteration frequencies from the breast invasive carcinoma (TCGA Firehose Legacy) dataset for the 40 genes selected as AP-MS baits in this study. Each vertical gray column represents a patient, such that various genetic alterations of 40 genes in a given patient are indicated as seen at the bottom. In total, 93% (1028 of 1108) of BC patients have nonsynonymous mutation, chromosomal copy-number alteration (CNA), or mRNA or protein expression alteration in one or more of these 40 genes. Genes analyzed for both WT and mutant proteins are highlighted in yellow. Existing gene alterations in MCF7 and MDA-MB-231 are shown on the right. (**B**) The experimental workflow in which each bait was expressed in biological triplicate in three cell lines and subjected to AP-MS analysis. (**C**) Majority (78%) of the high-confidence PPIs identified in this study are not represented in a panel of public PPI databases (CORUM, BioPlex 2.0, IMEx, and BioGRID low throughput and

multivalidated). (**D**) The frequency of nonsynonymous mutations, chromosomal CNVs, or mRNA expression alterations of 10,000 random size-matched permutations taken from the list of genes detected in the global protein abundance analysis. The white circle indicates the median of the random sampling, and the gray bar represents ±1 standard deviation. The frequency of alterations found in the prey retrieved in our PPI dataset is indicated in the black circle. (**E**) Venn diagram illustrating the overlap of PPIs (PPI score ≥ 0.9) across the three cell lines. PPI score is an average of the PPI confidence scores calculated from compPASS and SAINTexpress (see Materials and methods for details). The frequency of non-synonymous mutations of the prey genes in each sector of the Venn diagram was compared with those of 10,000 random size-matched permutations, as in (D). The P values for mutation enrichment in each prey set are shown in a color scale, where a stronger red represents more significant mutation enrichment.

alterations—documented in the BC TCGA cohort. Accordingly, we calculated the average frequency of each alteration for prey proteins detected in our PPIs compared with background expectation (fig. S1C and table S5). We observed that BC-associated mutations were significantly enriched in BC PPIs but that CNVs and mRNA expression alterations were not (Fig. 1D)—a trend that was also observed in head and neck squamous cell carcinoma (36). Furthermore, we found enrichment of tumor mutations in preys detected specifically in either of the two cancer cell lines (MCF7 and MDA-MB-231) among BC patient tumors but not in the preys of noncancerous MCF10A cells (Fig. 1E and table S4). This result supports the notion that the interaction partners of frequently altered cancer proteins are also under positive pressure for mutations. Along this line, in a prior study, we had compared the preys of frequently mutated baits to those of infrequently mutated baits from the BioPlex dataset and had found the same trend to emerge for almost all cancer types (33).

Out of 589 PPIs identified, 81% were not shared with other cell lines, which reflects a high cell-type specificity of PPIs in different genetic contexts (Fig. 1E). We speculated that differential protein abundance across cell lines might provide one explanation for cell type–enriched PPIs. However, although some changes in interaction could be explained by changes in protein abundance, we also found many cases with the opposite behavior, in which a gain in interaction was observed with a concomitant decrease in protein abundance (table S5 and fig. S1D).

Cell type–enriched interactions

To compare PPIs across cell lines, we defined a cancer-enriched differential interaction score (DIS) as the probability of the PPI being present in a cancer cell line (either MCF7 or MDA-MB-231) but absent in the normal cell line (MCF10A) (Materials and methods). Given that each PPI has a specific DIS, a continuous color scheme was used to represent cancer versus noncancer differential interactions. We used the results of this differential scoring analysis to visualize the entire BC PPI network showing PPIs that are (i) enriched in a cancer cell line, (ii) enriched in noncancerous MCF10A cells, or (iii) conserved in the two cancer cell lines but absent in the noncancerous context (Fig. 2 and table S6).

Among interactions enriched in a cancer cell line, we found the HRAS proto-oncogene and the tumor suppressor kinase STK11 (also known as LKB1) to interact with a set of DNA damage response (DDR) proteins (PDS5A, FANCI, MMS19, and GPS1) in MCF7 and MDA-MB-231 cells, respectively (Fig. 2B). The HRAS-FANCI and STK11-MMS19 interactions were further assessed using a proximity ligation assay (PLA). Abundant PLA spots were observed when both HRAS and FANCI antibodies were

incubated with fixed MCF7 cells, but either antibody alone generated only a background level of signal (Fig. 2, C and D, and fig. S2A), confirming the interaction seen by AP-MS. Also consistent with the mass spectrometry results, a significantly higher number of HRAS-FANCI PLA spots were detected in MCF7 compared with MDA-MB-231 and MCF10A cells (Fig. 2D). Again consistent with the cell-type specificity uncovered through AP-MS, STK11-MMS19 PLA spots were observed with consistently higher numbers in MDA-MB-231 than those in MCF7 and MCF10A cells (Fig. 2, E and F, and fig. S2A). We also observed the HRAS-FANCI and STK11-MMS19 interactions in two additional BC cell lines (T47D and SKBR3) by PLA (fig. S2, B and C). Analysis using three-dimensional (3D) segmentation revealed that the PLA spots are present in the cytoplasm as well as the nucleus (Fig. 2G and fig. S2, B and C), indicating nuclear roles of HRAS and STK11, potentially involving DDR and/or DNA repair functions based on their PPIs. Consistent with our findings, the Human Protein Atlas (www.proteinatlas.org) reveals that HRAS and STK11 are present both in the nucleus and cytosol based on immunofluorescence microscopy (37). Given the previous observations that the silencing of HRAS and STK11 leads to defective DNA repair and genome instability (38), these interactions may provide insights into direct effectors by which HRAS and STK11 modulate DDR. STK11 also interacted with cell adhesion factors in MCF10A cells (PLEKHA7 and PKP4; Fig. 2B), consistent with its role in cell autonomous polarization (39) and actin filament assembly at the cellular leading edge (40). Notably, CDH1 but not STK11 was found to interact with cell adhesion factors in MDA-MB-231 cells. CDH1 plays critical roles as a master regulator of cell-cell adhesion via adherens junctions, cell polarity, and cell migration (41), and abrogation of CDH1 expression is a hallmark of the epithelial-to-mesenchymal transition (42). The observed interaction patterns suggest that STK11 may contribute to cell polarity and focal adhesion through a physical interaction with PLEKHA7 and PKP4 but that it requires the cellular ability to form adherens junctions. This may explain the lack of interaction of STK11 with PLEKHA7 and PKP4 in MDA-MB-231 cells, which do not express CDH1 because of promoter hypermethylation (43).
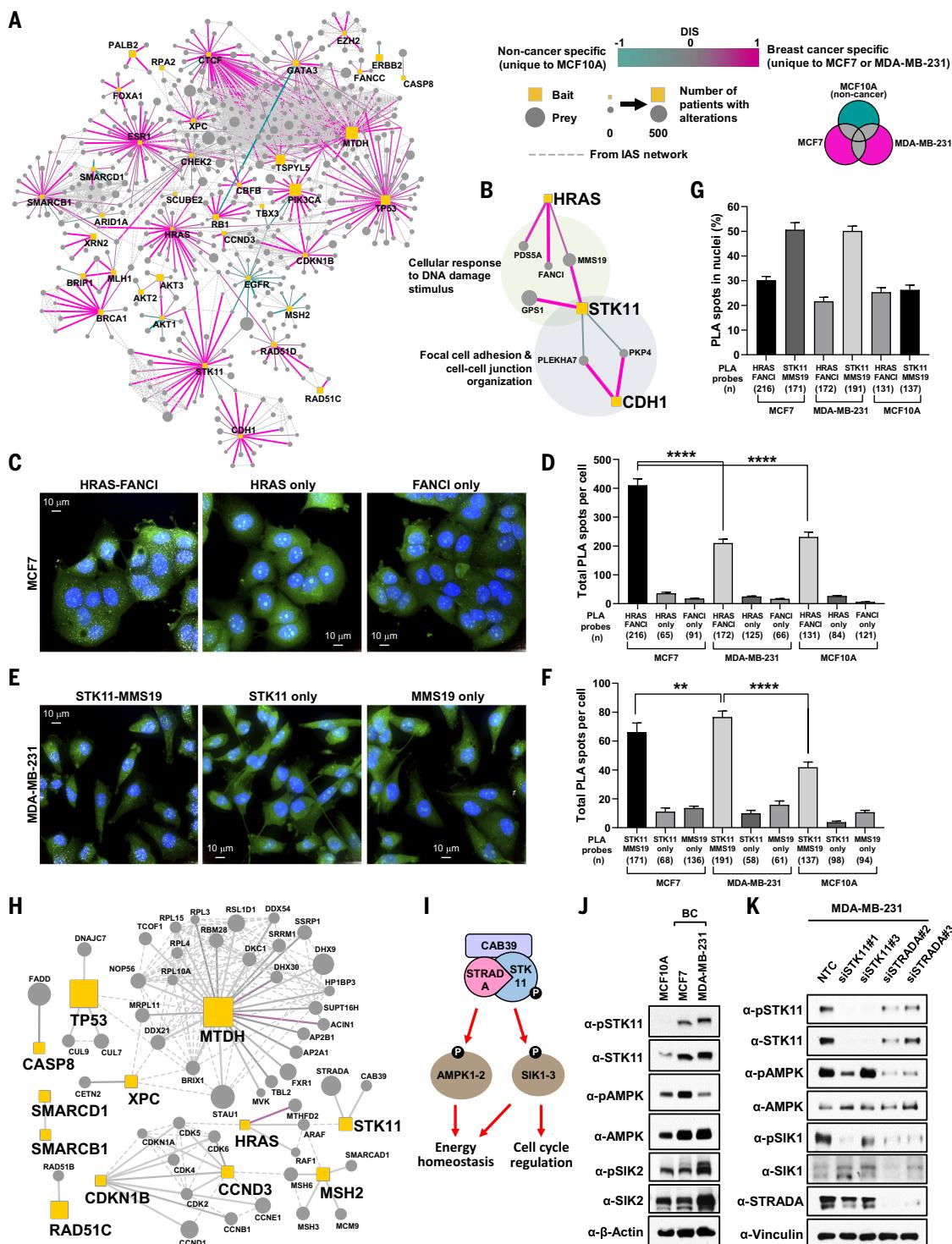
We also found that STK11 interacts with STRADA and CAB39 (also known as MO25) preferentially in the two cancer cell lines (Fig. 2H). STRADA and CAB39 form a heterotrimeric complex with STK11 (44) to properly position the activation loop of STK11 in an active conformation (45), which enables STK11 to phosphorylate and activate downstream kinases, including adenosine 5′-monophosphate (AMP)–activated protein kinases (AMPKs) and salt-inducible kinases (SIKs) involved in en-

ergy homeostasis and cell cycle regulation (Fig. 2I) (46–48). The increased associations among STK11, CAB39, and STRADA (regardless of protein abundance in these cells) suggests that STK11 activity is generally augmented in cancer. Consistent with this hypothesis, we found that both total and activated STK11 (phosphorylated at S428) are more abundant in MCF7 and MDA-MB-231 than in MCF10A cells (Fig. 2J). Furthermore, phosphorylation of STK11 downstream targets, including SIK2 and AMPK, was higher in either of the two BC cell lines (Fig. 2J). Knockdown of STRADA by two different individual small interfering RNAs (siRNAs) significantly reduced phosphorylation of STK11 (S428), AMPK (T172), and SIK1 (T182) in MDA-MB-231 cells (Fig. 2K), providing further evidence that the association of STK11 with STRADA contributes to downstream signaling of activated STK11. Increased STK11 activity may support cellular fitness by balancing energy production with anabolic metabolism, as previously seen in hepatocellular carcinoma (49).

Previously unidentified regulators of PIK3CA signaling

PIK3CA and *AKT* activating mutations and copy-number amplifications are frequently found in many cancer types, including BC (50–52), which indicates that the PI3K-AKT pathway is a key signaling module for cancer cell proliferation and thus an attractive target for therapeutic intervention (53). However, given the substantial role of the PI3K pathway in tumorigenesis, mechanisms of regulation or tuning by interacting proteins remains largely unknown because prior research predominantly centers around how mutations and alterations in the *PIK3CA* and *AKT* genes themselves regulate pathway activity.

Activation of PIK3CA by receptor tyrosine kinase (RTK) or oncogenic mutations leads to membrane recruitment and activation of AKT (Fig. 3A) (54, 55). In BC, mutations at the E545 and H1047 residues are most frequently found (Fig. 3B). Using AP-MS, we identified 20 prey proteins that interact with PIK3CA, 18 of which were observed in MCF7 cells (table S4). Of the 18 proteins, only four (IRS1, PIK3R1, PIK3R2, and PIK3R3) were previously known interactors (56–59). Many of these previously unknown PPIs are significantly decreased, and in some cases completely abolished, by different *PIK3CA* mutations (Fig. 3C). To determine whether these PIK3CA interactors modulate the PI3K-AKT pathway, we tested whether depletion of each target by siRNAs affects downstream AKT activation in MCF7 cells by measuring cellular phospho-AKT (pS473) levels in an in-cell Western assay (60). Four independent siRNAs per target gene were pooled and transfected for knockdown (Materials and methods). Nontargeting control

Fig. 2. Differential interaction analysis of the BC-enriched interactome.
(**A**) Interactome of the union of all high-confidence PPIs detected across all cell lines. Edges are colored on the basis of their differential interaction, with pink edges representing PPIs that are enriched to BC cell lines (unique to either MDA-MB-231 or MCF7) as compared with MCF10A cells (shown in teal edges). Dotted line represents the physical protein-protein association (validated in other studies) with high integrated association stringency score. (**B**) PPIs connecting HRAS, STK11, and CDH1. HRAS and STK11 have several interactors, including FANCI and MMS19 in BC cells, involved in cellular response to DNA damage stimulus. STK11 and CDH1 interact with PKP4 and PLEKHA7 in a

cell type–specific manner, implying differential regulation of cell adhesion and cell-cell junction in non-BC and BC cells. (**C**) Representative images of MCF7 cells from the PLA between HRAS and FANCI antibodies. Maximum intensity projection images are shown to represent total PLA interactions. PLA with only one of the two primary antibodies was performed as negative control. PLA spots (white), HCS CellMask Green stain (green) and 4′,6-diamidino-2-phenylindole (DAPI) (blue). Scale bar, 10 μm. (**D**) Total PLA spots per cell using HRAS and FANCI antibodies were quantified in MCF7, MDA-MB-231, and MCF10A cells. n indicates the total number of cells analyzed in each condition. ****$P \leq 1.0 \times 10^{-4}$. (**E**) Representative images of MDA-MB-231 cells from the PLA between

STK11 and MMS19 antibodies. (**F**) Total PLA spots per cell using STK11 and MMS19 antibodies were quantified in MCF7, MDA-MB-231, and MCF10A cells. ****$P \leq 1.0 \times 10^{-4}$; **$P \leq 1.0 \times 10^{-2}$. (**G**) Percent nuclear PLA spots in each PLA condition. (**H**) High-confidence PPIs that are commonly detected only in two cancer cell lines (MDA-MB-231 and MCF7) but not in noncancerous MCF10A cells. Node and edge styles and colors are the same as in (A). (**I**) STK11 forms a heterotrimeric complex with CAB39 and STRADA to activate its kinase activity and phosphorylate downstream kinases, including AMPK and SIKs, for regulating energy homeostasis and cell cycle. (**J**) STK11 kinase

activity was monitored by measuring total and phosphorylation levels of its known downstream substrates (AMPK and SIK2) as well as itself. The following phospho-epitopes were detected by antibodies: pSTK11 (pS428), pAMPKα (pT172), pSIK2 (pT175). (**K**) Knockdown of STK11 and its interacting protein (STRADA) by two individual small-interfering RNAs reduces phosphorylation of STK11 (S428), AMPK (T172), and SIK1 (T182). Single-letter abbreviations for the amino acid residues are as follows: A, Ala; C, Cys; D, Asp; E, Glu; F, Phe; G, Gly; H, His; I, Ile; K, Lys; L, Leu; M, Met; N, Asn; P, Pro; Q, Gln; R, Arg; S, Ser; T, Thr; V, Val; W, Trp; and Y, Tyr.

siRNAs (NTCs) as well as siRNAs targeting PIK3CA (a positive regulator) and PTEN (a negative regulator) were included as controls (*61*). As expected, knockdown of PIK3CA in MCF7 cells significantly diminished pAKT signal, whereas knockdown of PTEN augmented it (Fig. 3D, fig. S3A, and table S7). Knockdown of the PIK3CA interactors BPIFA1 and SCGB2A1 (also named PLUNC and mammaglobin-B, respectively) increased pAKT activity to a degree higher than or the same as the PTEN knockdowns, indicating that these two proteins are negative regulators of the PI3K-AKT pathway (Fig. 3D, fig. S3A, and table S7). To verify these in-cell Western results, we performed pooled and individual siRNA-mediated knockdown of BPIFA1 and SCGB2A1 and confirmed the increase of AKT pS473 by standard Western blot analysis in MCF7 cells (Fig. 3E and fig. S3B). Although BPIFA1 and SCGB2A1 were below the level of detection by the PIK3CA AP-MS in MDA-MB-231 cells (table S3), pooled and individual siRNA-mediated knockdown of BPIFA1 and SCGB2A1 in MDA-MB-231 cells also led to an increase in AKT pS473 (Fig. 3F and fig. S3C). These results suggest that BPIFA1 and SCGB2A1 may act as regulators of the PI3K-AKT pathway in multiple cellular contexts. Consistent with this, the interaction of BPIFA1 with 3xFLAG-tagged PIK3CA [wild-type (WT)] was confirmed by PLA in not only MCF7 but also MDA-MB-231 cells (fig. S3D), albeit at lower levels. Furthermore, abundant PLA spots between BPIFA1 and endogenous PIK3CA were also observed in T47D and SKBR3 cells (fig. S3E). To verify a negative role of BPIFA1 and SCGB2A1 in PIK3CA signaling, we measured their effect on the PIK3CA kinase activity in a reconstituted in vitro assay using recombinant proteins (PIK3CA/PIK3R1, BPIFA1, and SCGB2A1) and lipid substrate (phosphoinositol-4,5-bisphosphate) (Materials and methods). Consistent with the AP-MS results (Fig. 3C), increasing amounts of recombinant BPIFA1 and SCGB2A1 preferentially inhibit WT PIK3CA kinase activity toward lipid substrate when compared with the two mutant forms of PIK3CA (E545K and H147R) (Fig. 3, G and H). These data both confirm the validity of the PPI and provide further verification of the WT versus mutant specificity revealed by the AP-MS.

Effect of pathogenic mutations on the BRCA1 interactome

BRCA1 is a major hereditary cancer susceptibility gene (*62*, *63*) that plays critical roles in DNA repair by homologous recombination (HR) (*64*) in addition to other processes, such as regulation of transcription, RNA splicing, and the cell cycle (*65*, *66*). BRCA1 carries out its functions in concert with other proteins (*64*), leading to many studies of BRCA1-containing complexes and their roles in DNA repair (*67*, *68*). To date, many of these findings have been based on either immunoprecipitation with antibodies against the WT BRCA1 protein or interrogation of pairwise protein interactions with the yeast two-hybrid system. Moreover, these analyses have been done mainly using WT BRCA1 protein and have not systematically captured how different mutations in *BRCA1* might affect its protein interactions.

To comprehensively catalog the BRCA1 interactome and how pathogenic *BRCA1* mutations alter these interaction profiles, we performed AP-MS on WT and pathogenic variants reported in cancer patients, including C61G and R71G in the N-terminal RING domain (*69*, *70*) and S1655F as well as 5382insC and M1775R in the C-terminal tandem BRCT domain (*71*, *72*) (Fig. 4A). Given that alternative splicing in cancer often generates BRCA1 isoforms lacking exon 11, which confers residual HR activity and therapeutic resistance (*73*), an isoform (isoform 6; UniProt identifier P38398-6) lacking exon 11 with a distinct C terminus was also included in the analysis. The I26A separation of function mutation in the RING domain, which abrogates E3 ubiquitin (Ub) ligase activity but retains BARD1 binding, was also analyzed (*74*). We induced the expression of these BRCA1 proteins in all three breast cell lines; however, only MDA-MB-231 cells (harboring the *TP53* R280K mutation) supported ectopic 3xFLAG-BRCA1 expression. These observations were consistent with previous studies which have shown that ectopic overexpression of BRCA1 (in both wild type and mutants) is not stably maintained without a compensatory *TP53* mutation (*75*). AP-MS experiments in MDA-MB-231 cells identified 128 high-confidence interactions from eight BRCA1 constructs (the wild type and 7 mutants; PPI score ≥ 0.65; fig. S4A and

table S8); of these interacting proteins, 70 showed at least an eightfold change (Fig. 4B and fig. S4B).

These data revealed a number of previously unidentified BRCA1-interacting proteins along with known interactors, many of which were differentially affected by mutations in different domains of BRCA1. For example, HR proteins previously known to interact with BRCA1 (including BRIP1 and RBBP8) (*72*, *76*) had a similar pattern of interaction loss (boxed in green in Fig. 4B) associated with BRCT domain mutants (S1655F, 5382insC, and M1775R), whereas RING domain mutants (I26A, C61G, and R71G) maintained these interactions. In a separate pattern, we found that the C61G RING domain mutant abolishes interaction with BARD1 (Fig. 4B), as previously reported (*67*). Several interactions could be confirmed by coimmunoprecipitation and Western blot analysis (Fig. 4C). These results suggest that RING domain mutants are hypomorphic and may retain some BRCA1 functions, which could explain at least in part why the BRCA1 C61G variant is only moderately sensitive to cisplatin and poly(ADP-ribose) polymerase inhibitors (PARPi's) and becomes readily resistant to these drugs (*77*, *78*).

A Ub E2–conjugating enzyme, UBE2N (also known as UBC13), was found to interact with WT BRCA1 but to a lesser degree with mutant forms of BRCA1 (PPI score < 0.6) (boxed in sky blue in Fig. 4B). For example, consistent with reports from yeast two-hybrid studies (*79*), we found a sixfold reduction in UBE2N associated with the I26A mutant compared with the wild type, suggesting that UBE2N interacts with BRCA1 through the RING domain. Notably, the M1775R mutation in the BRCT domain also markedly reduced the interaction with UBE2N (Fig. 4B), suggesting that the M1775 residue in the BRCT domain may also contribute to the interaction with UBE2N, although the underlying mechanism is currently unclear. Depletion of UBE2N shows HR defects including altered RAD51 filament formation and E3 Ub ligase function of BRCA1 (*80*), indicating a critical role of UBE2N in HR repair. Consistent with the cell line models, we found that baseline UBE2N mRNA expression was significantly lower in patients who achieved pathologic complete response (pCR) to the PARPi (veliparib)
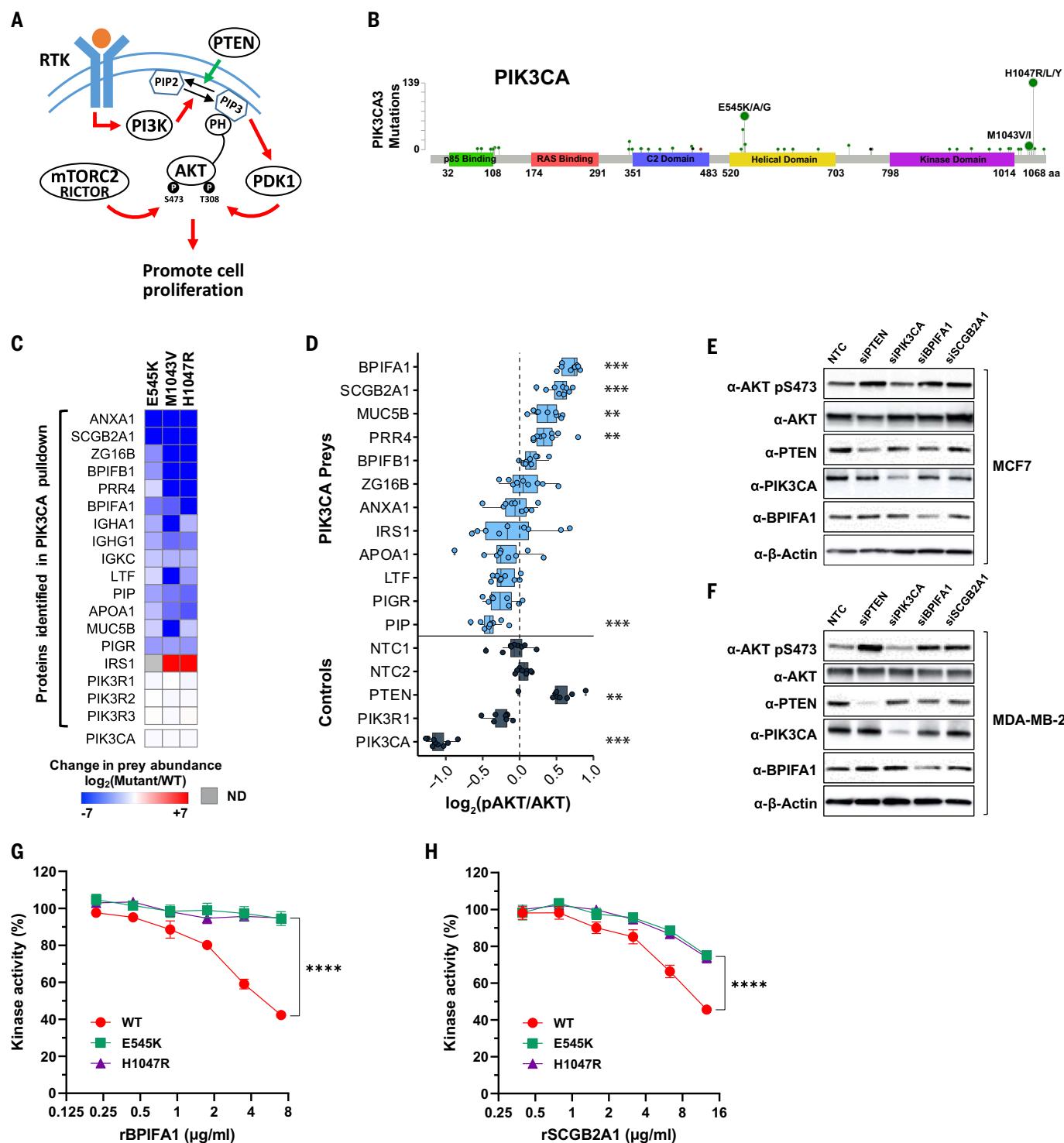
Fig. 3. Comparative interactome analysis of WT and mutant PIK3CA proteins. (**A**) Overview of the receptor tyrosine kinase (RTK)–PI3K signaling cascade leading to the phosphorylation (T308 and S473) and activation of the AKT pathway. (**B**) A lollipop plot representing the sites of *PIK3CA* mutations and the number of BC patients bearing a given *PIK3CA* mutation from TCGA (Firehose Legacy) study. (**C**) Relative quantification of the abundance of high-confidence preys observed from pull-down of PIK3CA (wild type and mutants) in MCF7 cells. Preys detected only in wild type are represented in deep blue, and preys detected only in mutants are represented in deep red. All three PIK3CA mutants were expressed and detected at a similar level. ND, not detected. (**D**) The level of AKT S473 phosphorylation (as

proxy of activation) was measured by in-cell Western analysis upon siRNA-mediated knockdown of PIK3CA-interacting preys and control genes (*PTEN*, *PIK3CA*, and *PIK3R1*) in MCF7 cells. The intensity of AKT pS473 was normalized to total AKT as well as cell viability. ***$P \leq 1.0 \times 10^{-3}$; **$P \leq 1.0 \times 10^{-2}$. (**E** and **F**) Increase of AKT S473 phosphorylation upon knockdown of BPIFA1 and SCGB2A1 was confirmed by Western blot in both MCF7 and MDA-MB-231 cells, respectively. (**G** and **H**) PIK3CA (WT, E545K, and H1047R) kinase activity toward phosphatidylinositol-4, 5-bisphosphate (PIP₂) was measured in vitro in the presence of increasing amounts of recombinant BPIFA1 and SCGB2A1, respectively. Results are from at least three to six independent experiments. ****$P \leq 1.0 \times 10^{-4}$.
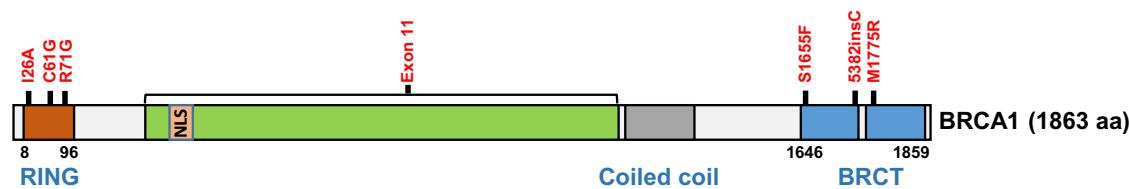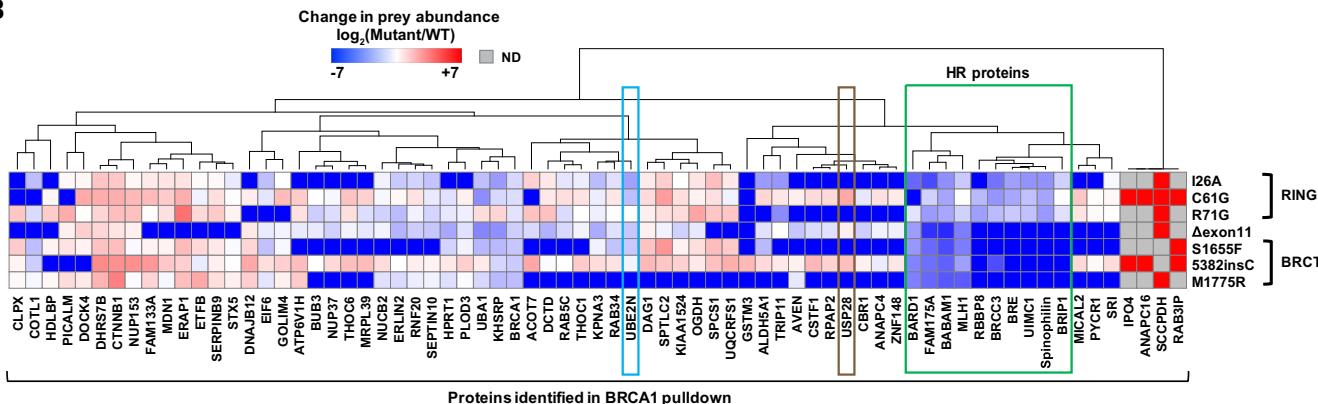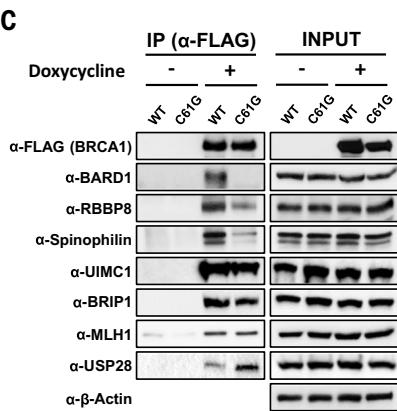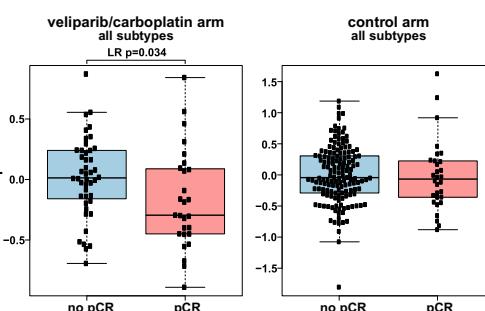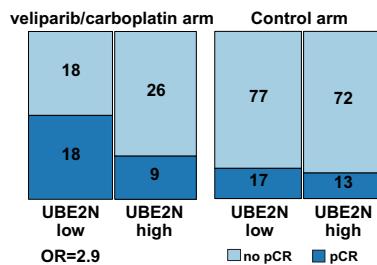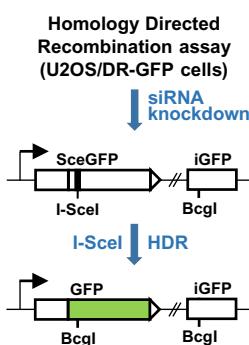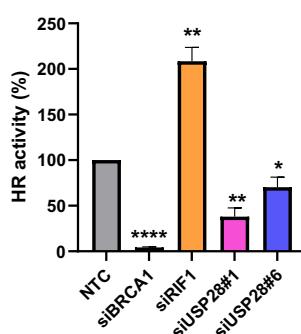
Fig. 4. Quantitative analysis of the effect of mutations on the BRCA1 interactome. (**A**) Functional domains in the *BRCA1* gene and the location of mutations analyzed by AP-MS. (**B**) Relative quantification of the abundance of prey proteins (PPI score ≥ 0.65; ≥8-fold change) identified by BRCA1 AP-MS in MDA-MB-231 cells. All prey abundance values were normalized by 3xFLAG-tagged BRCA1 levels in their respective AP-MS experiments. Preys detected only in wild type are represented in deep blue, and preys detected only in mutants are represented in deep red. A group of proteins involved in HR repair (boxed in green) are clustered together, wherein RING domain and BRCT domain BRCA1 mutants show distinct PPI abundance profiles. Spinophilin has

not previously been known to have a function relevant to HR repair. UBE2N is boxed in sky blue. USP28 is boxed in brown. ND, not detected. (**C**) PPIs of selected proteins with BRCA1 (WT or C61G mutant) were confirmed by coimmunoprecipitation with anti-FLAG antibody followed by Western blot analysis. (**D**) Box plot shows that the patient group (enrolled in the I-SPY 2 clinical trial) with pCR to veliparib (PARPi) and carboplatin (VC) had pretreatment tumors with significantly lower UBE2N mRNA expression (LR $P = 0.034$) than those of nonresponding patients. By contrast, BC patient tumors in the control arm did not show any significant difference in UBE2N expression between pCR and no-pCR groups. (**E**) Mosaic plot shows that BC patients who did pCR to VC in addition to

standard chemotherapy were 2.9 times as likely to have lower mRNA expression of UBE2N in their pretreatment tumors (odds ratio = 2.9). In the control arm, there is no significant difference in pCR between low and high UBE2N expression groups. Numbers in each block represent the patient sample size. Column width indicates the relative proportion of the UBE2N low and high expression group on the patient population. (**F**) A schematic of the HR reporter assay. The DR-GFP reporter contains two defective copies of the GFP gene, one disrupted by an I-SceI site and the other lacking a promoter. I-SceI cutting of the first

copy generates a DSB, and repair by HR with the second copy as a template leads to restoration of a functional GFP gene. siRNA-mediated knockdown of HR-related genes leads to reduction of GFP+ cells (a proxy of HR activity) compared with NTC experiments. (**G**) HR activities upon depletion of USP28 relative to NTC (set to 100%). Depletion of BRCA1 and RIF1 was included and analyzed as controls. Data shown are the means from three to six independent experiments for each siRNA. Error bars represent standard deviations (SDs). ****$P \leq 1.0 \times 10^{-5}$; **$P \leq 0.01$; *$P \leq 0.05$.

and carboplatin (*81*) compared with nonresponsive patients (*P* = 0.034; Fig. 4D) in I-SPY 2, a neoadjuvant, adaptive clinical platform trial for high-risk early-stage BC (*82*). By contrast, BC tumors in the control arm did not show any significant difference in UBE2N expression between pCR and no-pCR groups. Although the average expression of UBE2N is numerically lower in TN than HR+HER2− tumors, the difference is not statistically significant (*P* = 0.1; fig. S4C). Moreover, the association of low UBE2N expression to pCR is seen more strongly in the HR+HER2− subset (*P* = 0.0012; fig. S4D) than in the population as a whole (*P* = 0.034; Fig. 4D), which suggests that the association is not merely a proxy for the TN subtype. *BRCA1* and *BRCA2* (*BRCA1/2*) germline mutation status is available for 112 of 115 patients in the veliparib and carboplatin (VC) and concurrent control arms, and 15 of 112 (13%) are *BRCA1/2*−. UBE2N trends toward lower expression levels in *BRCA1/2* mutation carriers (*P* = 0.07; fig. S4E). However, in the HR+HER2− subset (*n* = 55 with *BRCA1/2* mutation status data), where lower UBE2N levels associate with response to VC, there are only four mutation carriers and no difference in UBE2N levels by *BRCA1/2* status (*P* = 1). Furthermore, only two HR+HER2− *BRCA1/2* mutation carriers were treated by VC (only one of these achieved pCR), which implies that association between UBE2N and pCR in this subset may not be driven by spurious association with germline *BRCA1/2* mutation (fig. S4F). These results indicate that expression of UBE2N may serve as a biomarker of response to PARPi's and other DNA repair targeted therapies (odds ratio = 2.9; Fig. 4E). Notably, there are several observations that not all of BRCA1-interacting HR proteins show a response to PARPi upon depletion (by CRISPR or siRNA) when tested in multiple cell line models, as seen in a recent CRISPR screen (*83*). Furthermore, the clinical response of many BRCA1-interacting proteins to PARP inhibition has never been explicitly tested in a clinical setting. Therefore, identification of UBE2N as a potential biomarker for PARPi response could be clinically valuable to help stratify patients with UBE2N alteration for targeted therapy.

A deubiquitinase USP28 was found to interact more strongly with the BRCA1 mutants C61G and 5382insC than the wild type by AP-MS (boxed in brown in Fig. 4B), and this dif-

ferential interaction was confirmed by coimmunoprecipitation and Western blot analysis (Fig. 4C). USP28 was previously known to stabilize multiple DDR proteins (e.g., CHEK2, CLSPN, NBS1, and TP53BP1) in response to DNA damage (*84, 85*), and its recruitment to DNA double-strand breaks (DSBs) was shown to be dependent on the tandem BRCT domain of TP53BP1 (*86*). To further delineate the role of USP28 in DNA DSB repair, we analyzed the effect of USP28 knockdown on HR activity. In this assay, DNA DSBs were induced by I-SceI endonuclease, which cleaves nonfunctional green fluorescent protein (GFP) cassettes engineered in the genome of U2OS reporter cell lines (DR-GFP) (*87*). DSB repair that depends on the HR mechanism restores a functional GFP gene, yielding a readout tied to fluorescent signal intensity (Fig. 4F). Upon USP28 knockdown by siRNA, HR activity was significantly reduced when compared with NTC (Fig. 4G and fig. S5A), which suggests that USP28 is regulating proper HR repair. In the same assay, knockdown of BRCA1 greatly decreased HR as expected (*88*), whereas depletion of RIF1, a protein functioning in an alternative nonhomologous end joining DNA repair pathway, did not. To identify proteins potentially regulated by USP28 through deubiquitination, we performed a global ubiquitome analysis upon knockout (KO) of *USP28* in MDA-MB-231 cells by CRISPR-Cas9 ribonucleoprotein (RNP) strategy (*89*). Polyclonal *USP28* KO cells with ~85% KO efficiency (crRNA3; fig. S5B) as well as control (NTC) cells were lysed, and ubiquitinated peptides were subsequently enriched and analyzed by mass spectrometry. Functional enrichment analysis of 275 Ub-enriched proteins observed in *USP28* KO cells compared with control cells [log$_2$ fold change (log$_2$FC) ≥ 1; *P* ≤ 0.05; table S9] revealed that 19 proteins (7%) belong to the cellular response to stress category (Gene Ontology: 0033554) (fig. S5C), and subsequent analysis further categorized proteins involved in cellular response to DNA damage stimulus (eight proteins) (fig. S5, D and E). Notably, these include ubiquitylation-dependent DDR signaling proteins (UBA1, RAD18, and DDB2) (*90–92*) and DNA replication helicases (MCM3 and MCM6) (*93*), which provides further evidence for a role of USP28 in responding to DNA damage and replication stress in cells.

Spinophilin is a previously unidentified BRCA1-interacting protein

Another protein interacting with BRCA1 in a mutation-dependent manner is spinophilin (encoded by *PPP1R9B*), a neuronal scaffolding protein that regulates synaptic transmission through its ability to target protein phosphatase 1 (PP1) to dendritic spines, where it inactivates glutamate receptors (*94*). Binding of spinophilin to BRCA1 was abolished by BRCT domain mutations similar to the pattern observed earlier for HR proteins (Fig. 4B). Reciprocal AP-MS was performed using 3xFLAG-tagged spinophilin in MDA-MB-231 cells, which confirmed the interaction of spinophilin with BRCA1 as well as with PP1 catalytic subunits (PPP1CA, PPP1CB, and PPP1CC) (Fig. 5A). MSstats analysis of differential interactions between BRCA1 WT and BRCT domain mutants demonstrated that an intact BRCT domain is required for the BRCA1-spinophilin interaction (fig. S6A). In fact, spinophilin was previously observed but unexplored in a systematic analysis of proteins interacting with the BRCT domain of BRCA1 (*95*). The BRCA1 BRCT domain binds to a pS-x-x-F motif on target proteins (*96*), and such recognition has been reported for BRCA1 interactions with FAM175A, BRIP1, and RBBP8 (*72, 76, 97*). Notably, spinophilin has three potential pS-x-x-F recognition motifs at S212, S248, and S635. To map the BRCT domain-binding motif on spinophilin, we mutagenized serine residues into alanine at each pS-x-x-F site and transfected each spinophilin (HA-tagged) construct individually along with 3xFLAG-BRCA1 DNA construct into HEK293T cells. The association of each spinophilin mutant with BRCA1 was monitored after immunoprecipitation of spinophilin using anti-HA beads followed by Western blotting with anti-FLAG antibody. This experiment showed that the S635A mutant interacted significantly less with BRCA1, demonstrating that spinophilin requires the pS635PTF motif for binding the BRCT domain of BRCA1 (Fig. 5B and fig. S6B). The F451A mutation, which resides in the interface with PP1 RVXF binding groove, also significantly diminished the interaction of spinophilin with PP1 (PPP1CA) (Fig. 5B and fig. S6B), as has been observed previously (*98*).

The AP-MS experiment found that spinophilin interacts with additional proteins involved in DNA replication and repair, including MCM10 and WDR48 (Fig. 5A). These results
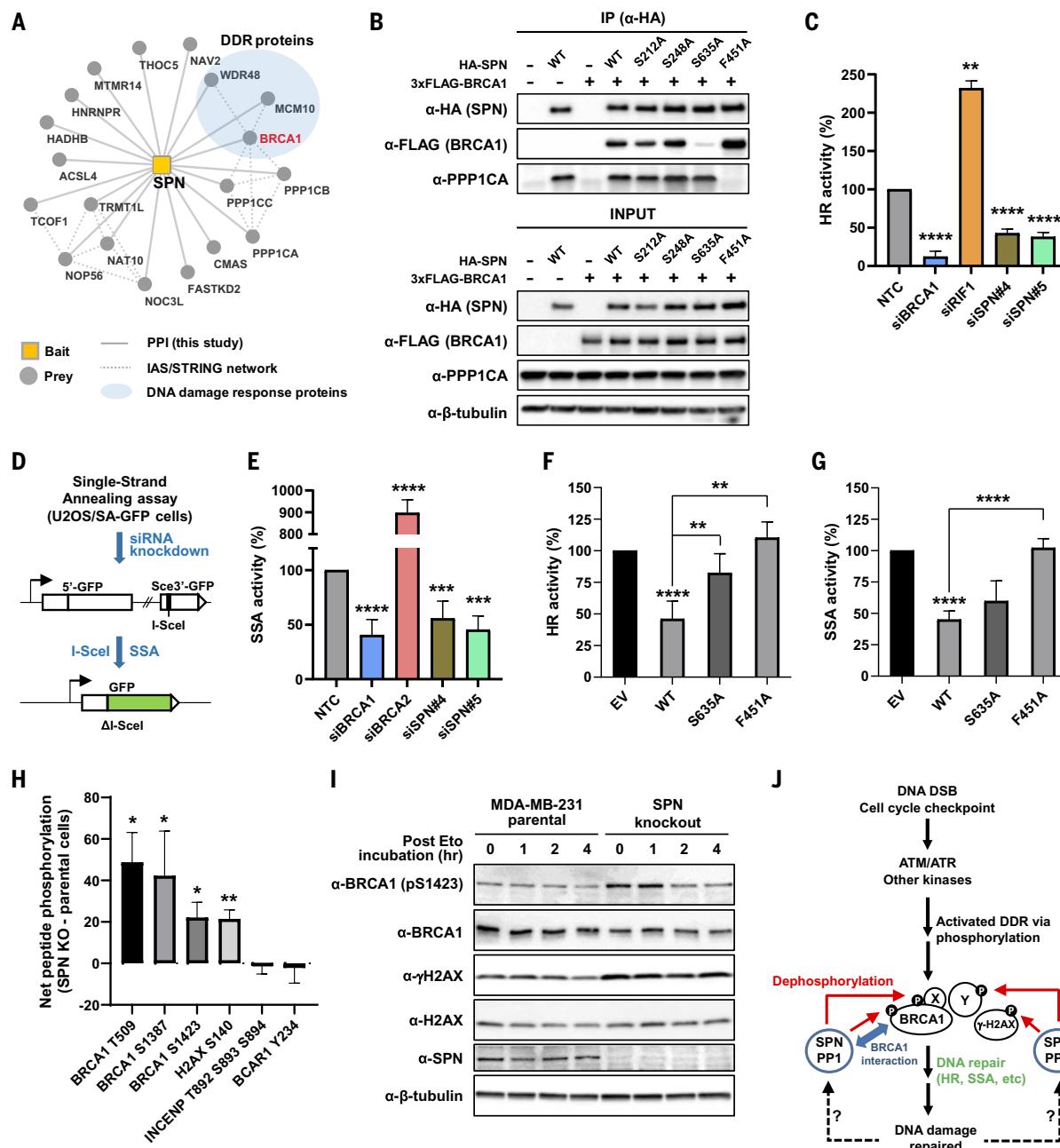
Fig. 5. Spinophilin interacts with BRCA1 and regulates DDR through dephosphorylation. (**A**) AP-MS of 3xFLAG-tagged spinophilin (SPN) (encoded by *PPP1R9B*) identifies BRCA1 (highlighted in a red edge) and other DDR-related proteins as well as PP1 catalytic subunits (PPP1CA, PPP1CB, and PPP1CC) in MDA-MB-231 cells. (**B**) HA-tagged SPN (WT, S212A, S248A, S635A, or F451A) was transfected with 3xFLAG-BRCA1 into HEK293T cells. After pull-down with anti-HA magnetic beads, coassociated 3xFLAG-BRCA1 was monitored. S635A mutation significantly diminished BRCA1 pull-down, whereas F451A mutation abolished the association with PP1 catalytic subunit (PPP1CA). Empty vectors were used as negative control. (**C**) HR activities upon depletion of SPN relative to NTC (set to 100%) were measured as in Fig. 4G. Data shown are the means from three to nine independent experiments for each siRNA. Error bars represent standard deviations (SDs). ****$P \le 1.0 \times 10^{-5}$; **$P \le 1.0 \times 10^{-2}$. (**D**) A schematic of the SA-GFP reporter assay. The SA-GFP reporter contains a 5′-fragment of GFP (5′-GFP) and a 3′-fragment of GFP (Sce3′-GFP) that contains an I-SceI site. Repair of the DSB in Sce3′-GFP using 266-nucleotide homology by SSA restores a functional GFP gene. (**E**) SSA activities upon depletion of SPN relative to NTC (set to 100%). Depletion of BRCA1 and

BRCA2 was included and analyzed as controls. Data shown are the means ± SDs from six independent experiments for each siRNA. ****$P \le 1.0 \times 10^{-4}$; ***$P \le 1.0 \times 10^{-3}$. (**F** and **G**) CMV promoter–driven SPN (WT, S635A, or F451A) expression DNA construct was transfected into U2OS DR and SA-GFP reporter cells, and the effect of SPN overexpression on HR and SSA activities was monitored, respectively. ****$P \le 1.0 \times 10^{-4}$; **$P \le 1.0 \times 10^{-2}$. (**H**) Selective peptides derived from various proteins including BRCA1 and H2AX as well as non-DNA repair proteins (INCENP and BCAR1) were individually mixed with lysates from either SPN KO or parental cells and subsequently monitored for phosphorylation by measuring ATP consumption in each reaction. Net peptide phosphorylation values are net changes in ATP concentrations between SPN KO cells and parental control cells (subtraction of parental runs from SPN KO runs). Mean value of two independent runs was shown on the *y* axis. Units are arbitrary. Error bars represent standard deviations (SDs). *$P \le 0.05$; **$P \le 1.0 \times 10^{-2}$. (**I**) SPN KO and parental cells were treated with 2.5 µM etoposide (Eto) for 16 hours and changes in the phosphorylation level of BRCA1 S1423 (pS1423) and H2AX S140 (γ-H2AX) were monitored at 0, 1, 2, and 4 hours after Eto treatment with fresh medium. (**J**) Model for the role of SPN in regulating DDR. See text for details.

suggest that spinophilin may participate in and/or regulate DNA repair by interacting with various DNA repair and replication proteins, including BRCA1. To explore this hypothesis, we analyzed the effect of spinophilin knockdown on DNA repair by HR and single-strand annealing (SSA). Upon spinophilin knockdown, HR activity was significantly reduced compared with NTC siRNA (Fig. 5C and fig. S6C). Similarly, knockdown of spinophilin significantly reduced SSA activity, comparable to BRCA1 depletion, whereas BRCA2 depletion markedly increased SSA, as seen previously (88) (Fig. 5, D and E, and fig. S6D), which implies that spinophilin promotes both HR and SSA-mediated DSB repair.

According to the breast invasive carcinoma patient cohort study by TCGA (2), there is no clear evidence that the spinophilin (PPP1R9B) gene is recurrently silenced by deep DNA copy loss or mutation. Using the interface to the TCGA methylation data (http://maplab.imppc.org/wanderer/), we did not observe evidence for methylation of the spinophilin (PPP1R9B) promoter, either. However, among the sequenced TCGA BC patient tumors that have alterations in the spinophilin (PPP1R9B) gene (73 of 1084), the majority (69 of 73) of the alterations are amplification, which suggests that higher expression of spinophilin may be a pathogenic driver of BC. We therefore also analyzed the effect of spinophilin overexpression (mimicking amplification) on HR and SSA DSB repair. CMV promoter–driven overexpression of WT spinophilin in the U2OS reporter cell lines led to significant reduction in both HR and SSA activities compared with that in the empty vector control (Fig. 5, F and G). Consistent with these observations, a recent study identified spinophilin as a BC oncogene (99). However, the effect of overexpression of the S635A mutant (incapable of interacting with BRCA1) on HR was significantly mitigated, and overexpression of the F451A mutant (incapable of interacting with PP1) did not affect HR or SSA at all (Fig. 5, F and G, and fig. S6, E and F), which implies that the inhibitory effect of WT spinophilin overexpression is likely exerted by PP1-mediated dephosphorylation and/or BRCA1 interaction (at least for HR).

To further unravel the biological function of spinophilin, we knocked out spinophilin in MDA-MB-231 cells using a CRISPR-Cas9 RNP method (89). Using genomic DNA polymerase chain reaction (PCR) followed by sequencing and Western blot analyses, at least two independent spinophilin KO clones were identified (fig. S7). We hypothesized that spinophilin targets PP1 to specific DNA repair proteins for dephosphorylation. To uncover potential dephosphorylation targets under this model, we used a high-throughput peptide phosphorylation assay platform (100). This system uses a collection of peptide sequences derived from biological targets of multiple kinases, which serves as phosphorylatable probes in a large-scale adenosine 5′-triphosphate (ATP)–consumption assay (101). In this assay, we measured changes in phosphorylation (i.e., ATP-consumption) of peptide substrates derived from various proteins, including BRCA1 and the DSB-associated histone H2AX as well as proteins unrelated to DNA repair (e.g., INCENP and BCAR1), in spinophilin KO and parental cells. We found that BRCA1 residues at T509, S1387, and S1423, as well as H2AX at S140 (γ-H2AX), were significantly increased in phosphorylation in spinophilin KO cell lysates compared with lysates from parental cells, and, in fact, were among the top 20 most increased sites (Fig. 5H and fig. S8A). BRCA1 pT509 enhances nuclear localization and transcriptional activity of BRCA1 (102), and pS1387 and pS1423 sites in the BRCA1 SQ-cluster region are critical for HR repair and cell-cycle checkpoint functions (103–105). γ-H2AX is a hallmark of DNA DSB (106) and initiates a signaling cascade to recruit various DSB repair proteins to properly repair the DNA damage (107). These results were in contrast to phosphorylation of the INCENP and BCAR1 peptides, which were not significantly changed by spinophilin disruption. To validate these results, spinophilin KO and parental cells were treated with 2.5 μM etoposide (Eto) for 16 hours to induce BRCA1 pS1423 and γ-H2AX, and persistence of these phosphosites was monitored by Western blot at 0, 1, 2, and 4 hours after Eto treatment. These phosphosites remained at a significantly higher level and were maintained for longer in spinophilin KO cells compared with parental cells (Fig. 5I). Consistently, we also observed higher levels of BRCA1 pS1423 and γ-H2AX after Eto treatment in spinophilin knockdown U2OS cells (fig. S8B).

To unbiasedly identify targets that are potentially dephosphorylated by spinophilin, we performed a phospho-proteomic analysis using the two spinophilin KO clones and parental MDA-MB-231 cells. In this experiment, we found that 473 phospho-peptides (from 407 proteins) were more than fourfold enriched (log2FC ≥ 2; $P \leq 0.05$) in both spinophilin KO clones compared with parental cells, whereas 328 phospho-peptides (from 280 proteins) were more than fourfold depleted (log2FC ≤ −2; $P \leq 0.05$) (fig. S9, A and B, and table S10). Notably, proteins known to be directly connected to BRCA1 through physical and/or functional interactions were significantly enriched in the group of up-regulated phospho-proteins seen in spinophilin KO cells (fig. S9C). Functional enrichment analysis of these 407 up-regulated phospho-proteins revealed that 32 proteins (8%) belong to the DNA repair category (Gene Ontology: 0006281) (fig. S9D), and subsequent analysis further categorized 15 proteins involved in DSB repair (fig. S9E). Notably, the 32 DNA repair proteins include not only BRCA1-interacting proteins

(e.g., BRIP1) but also contain key regulators of DNA repair pathways (e.g., MDC1 and TP53BP1) and helicase or nuclease (e.g., MRE11 and WRN), suggesting broad roles of spinophilin in modulating DNA repair and genome integrity (fig. S9, F and G). Taken together with the previous data, these results indicate that spinophilin regulates BRCA1 and DDR signaling by dephosphorylation (Fig. 5J).

Discussion

The cell is composed of a series of protein complexes, or machines (108), that function together in an elaborate network of pathways. Mutations, such as those seen in cancer, perturb the machines and therefore the network of pathways (109). Understanding the machines and networks in healthy and diseased states is crucial for a deeper understanding of disease biology and ultimately the discovery of new therapeutic strategies and the application of precision medicine (110). Using this premise as an underlying motivation, we generated comprehensive interaction maps for 40 frequently altered BC proteins. This large-scale study of biophysical interactions in BC and across three cell lines of human breast tissue origin provides a PPI resource to study BC biology and to contextualize uncharacterized mutations within signaling pathways and protein complexes. Approximately 78% of PPIs we identified have not been previously reported (Fig. 1C), and 81% are not shared across cell lines (Fig. 1E). The cell line PPI specificity we observe in this study and our accompanying manuscript (36), as well as that observed in a recent large-scale AP-MS study (27), speaks to the complexity of PPI networks and their heterogeneity among different cell types, calling for more studies to deeply characterize these networks in a wider range of cellular contexts. Given that each BC subtype arises by distinct tumorigenic mechanisms as a result of different genomic alterations, PPIs from cell lines representing other BC subtypes will most likely capture additional sets of interactors reflecting their distinct tumorigenic mechanisms. Our results also suggest that protein abundance in a cell line is not the sole mechanism for PPI specificity (fig. S1D). Presumably other features, such as differential posttranslational modifications (PTMs), cellular compartmentalization, and/or the mutational status of proteins, may contribute to cell type–specificity. Notably, prey proteins enriched to either of the two BC cell lines are more frequently mutated in breast tumors than preys from nontumorigenic cells (Fig. 1E), which implies that proteins interacting with cancer drivers may also contribute to the onset of cancer.

Using the systematic proteomic approach, we have identified previously unidentified interactors of PIK3CA that negatively regulate the PI3K-AKT pathway (Fig. 3, D to H). Notably,

RNA expressions of several of these interactors (e.g., BPIFA1, BPIFB1, and MUC5B) were found to be correlated in human airway epithelial cells ([111]), implying that they may be controlled under the same transcriptional regulatory program and/or be functionally related. Our results reveal that they play a role in the PI3K-AKT signaling cascade in the BC context. BPIFA1 is a lipid-binding protein with antimicrobial and immunomodulatory functions ([112]). It is significantly down-regulated in nasopharyngeal carcinoma ([113]), and its single-nucleotide polymorphisms (SNPs) are associated with increased susceptibility to this tumor type ([114]). BPIFA1 is known to increase the expression of PTEN through down-regulating the miR-141 oncogene ([115]); thus, knockdown of BPIFA1 could indirectly activate PI3K-AKT. The BPIFA1-PIK3CA interaction we identified and the inhibition of WT PIK3CA kinase activity by BPIFA1 in vitro suggests that BPIFA1 may also directly modulate PI3K-AKT via PPI, which warrants a structural study of the complex. Another PIK3CA interactor, SCGB2A1, is a small secreted protein highly differentially expressed in multiple types of cancer, including breast and endometrium ([116], [117]). Previous studies have shown that SCGB2A1 is expressed at lower levels in luminal BC compared with histologically normal breast epithelium ([118]) and that decreased SCGB2A1 expression in endometrial tumors is significantly correlated with higher grade lymph node metastasis, advanced stage cancer, and worse overall survival ([119]). Neither the BPIFA1 nor the SCGB2A1 gene harbors recurrent focal deep deletions, missense mutations, or truncating mutations in their coding regions among 996 breast tumors in TCGA analysis ([2]). However, SCGB2A1 harbored loss of heterozygosity (LOH) in 10% of breast tumors (7% LOH in all tumors) according to a recent study ([120]), which suggests that its allelic imbalance may contribute to the development of tumors.

We also uncovered a number of previously unidentified interactors of the well-studied BRCA1—which is tightly connected to DNA repair processes—including spinophilin. Notably, both knockdown and overexpression of spinophilin led to significant impairment in DSB repair by both HR and SSA pathways (Fig. 5, C and E to G), establishing that this protein has a defined role in DNA repair. An intriguing question is how the alterations of spinophilin expression interfere with HR and SSA repair activity. Given the role of spinophilin in dephosphorylation, one plausible explanation is that prolonged phosphorylation or prevailed dephosphorylation of BRCA1 and other DDR proteins is inhibitory to multiple steps during DNA repair, including DSB-end resection, which is a prerequisite for HR and SSA. In agreement with this hypothesis, continuous DNA damage signaling and phosphorylation of several DDR proteins (including H2AX, NBN, RPA2, and CHEK2) induced by short double-stranded DNA molecules (mimicking DNA DSB) was shown to disorganize the cellular DNA repair system and inhibit DSB repair ([121]). Alternatively, but not exclusively, spinophilin may play a role in initiating the DSB repair process by removing constitutive phosphorylations that inhibit the function of DDR proteins. Supporting this scenario, a phospho-proteomic study revealed that more than one-third of the captured phospho-peptides were dephosphorylated within minutes of DNA damage ([122]). Additionally, spinophilin may be involved in counteracting DSB-induced phosphorylation events, thus promoting the recycling of DDR proteins as DNA damage is being repaired, possibly through its interaction with BRCA1.

Finally, although the approach we described in this study was applied to BC, it is equally powerful against other cancers, including head and neck squamous cell carcinoma (HNSCC) ([36]). Efforts such as this will ultimately lead to hierarchical maps of protein complexes and systems in both healthy and diseased cells ([123]), which, based on the mutational landscape, can be predictive for use of known treatments and can also be used to uncover previously unidentified therapeutic strategies across a multitude of disease areas.

Materials and methods
Cloning and cell line generation

Complementary DNAs (cDNA) of each bait were obtained from human ORFeome collection (v8.1) or Addgene [pcDNA6-ARID1A (no. 39311), pcDNA3-Casp8 (no. 11817), hEcadherin-pcDNA3 (no. 45769), pDONR223_EGFR_WT (no. 81926), pDONR221-spinophilin (no. 87123)]. In case that cDNAs of canonical isoforms were not available, we synthesized them using gBlock fragments (IDT, Genewiz). These cDNAs were cloned using the Gateway Cloning System (Life Technologies) into a doxycycline-inducible N-term or C-term 3xFLAG-tagged vector modified to be Gateway compatible from the pLVX-Puro vector (Clontech). Point mutant baits were generated via site-directed mutagenesis. All expression vectors were full-sequence verified. Bait information can be found in table S2.

Cell culture, lentivirus production, and stable cell line generation

MDA-MB-231 (ATTC, HTB-26) cells were maintained in Dulbecco's modified Eagle's medium (DMEM) and Ham's F-12 50/50 (Corning) supplemented with 10% fetal bovine serum (Gibco) and 1% Penicillin/Streptomycin (Corning). MCF10A (ATCC CRL-10317) cells were maintained in DMEM and Ham's F-12 50/50 supplemented with 20% horse serum (Gibco), EGF (PeproTech), Hydrocortisone (Sigma-Aldrich), Cholera toxin (Sigma-Aldrich), Insulin (Sigma-Aldrich) and 1% Penicillin/Streptomycin.

HEK293T (ATCC, CRL-3216), MCF7 (ATCC, HTB-22) and U2OS-GFP reporter cell lines (gifts from J. Stark at City of Hope National Medical Center) were maintained in DMEM supplemented with 10% fetal bovine serum (Gibco) and 1% Penicillin-Streptomycin. All cells were cultured at 37°C in a humidified atmosphere with 5% CO_2.

One day before transfection, 5.0 million HEK293T cells were plated in a 15-cm dish. Lentivirus was produced for each protein by using 5 μg of expression vector, 3.33 μg of Gag-Pol-Tat-Rev packaging vector (pJH045 from Judd Hultquist) and VSV-G (pJH046 from Judd Hultquist) mixed with 30 μL of PolyJet DNA Transfection Reagent (SignaGen) in serum free DMEM. DNA complexes were incubated at room temperature (RT) for 25 min and added dropwise to HEK293T cells. After 72 hours, the lentivirus containing supernatant from infected HEK293T cells was centrifuged at $400 \times g$ for 5 min to pellet any debris. The supernatant was filtered through a 0.45 μm PVDF filter. Virions were let to aggregate and precipitate in PEG-6000 (8.5% final) and NaCl (0.3 M final) at 4°C for 4 to 8 hours. Virions were pelleted by spinning at 3500 rpm for 20 min at 4°C. The pellet was then resuspended in Dulbecco's phosphate-buffered saline (DPBS) for a final volume between 800 to 1000 μL and stored at −80°C until use.

Stable cell lines were generated by transducing a 10-cm plate at 80% confluency with 200 μL of precipitated lentivirus for 24 hours. Transduced cells were selected with 2.5 μg/mL of puromycin.

Cell lysis and affinity purification

Three independent biological replicates of cells were plated in 10-cm dishes. For doxycycline-inducible gene expression, we induced cells at 40 to 50% confluence with 1 μg/mL doxycycline for 40 hours. To prepare cell extracts, a 10-cm dish was washed with 1 mL of ice-cold PBS and lysed in 300 μL of S150 or S300 lysis buffer (50 mM Tris, pH 7.5, 150 or 300 mM NaCl, 1 mM EDTA, 0.5% NP-40, 1 mM DTT, 1X Protease and Phosphatase Inhibitor Cocktail and 125 U Benzonase/mL) using freeze thaw method: 5 min on dry ice, followed by 30 to 45 s thaw in 37°C water bath with agitation. Cell lysates were clarified by spinning at $13,000 \times g$ for 15 min at 4°C. A 20 μL aliquot was saved for Western blot.

For FLAG purification, 25 μL of bead slurry was washed twice with 1 mL of S150 buffer. Supernatants were incubated with Anti-FLAG M2 magnetic beads (M8823, Sigma-Aldrich) overnight at 4°C with rotation. The beads were washed one time with 1 mL of S150 buffer containing 0.1% NP40 followed by two washes in detergent free S150 buffer.

To perform on bead digestion, magnetic beads were resuspended in 15 μL of freshly

prepared 8 M urea with 50 mM Tris, pH 9.0, 1 mM DTT and 1 µg LysC and incubated for 1 hour at 37°C. Supernatant was incubated with 3 mM iodoacetamide (IAA) in the dark at RT for 45 min. Quenching IAA with 3 mM DTT for 15 min at RT was followed by another incubation for 1 hour at RT with shaking. Samples were diluted fourfold by 50 mM Tris, pH 8.0 to bring final concentration of urea to 2 M and digested with 1 µg trypsin at 37°C overnight. Samples were acidified with 10% trifluoroacetic acid (TFA) to final 0.5% (pH<2) and desalted using Nest C18 tips. Tips were equilibrated with 100 µL of 80% acetonitrile, 0.1% TFA and sequentially washed three times with 100 µL of 0.1% TFA. After applying samples, bound peptides were sequentially washed three times with 100 µL of 0.1% TFA and eluted with 140 µL of 50% acetonitrile and 0.25% formic acid (FA). Eluted peptides were dried under vacuum centrifugation and resuspended in 15 to 20 µL of 1% FA before mass spectrometry.

Global endogenous protein abundance and Ub or phospho-proteomic analysis

After cell lysis, protein concentration was determined using Bradford assay. IAA was added to each sample to a final concentration of 10 mM, and samples were incubated in the dark at room temperature for 30 min. Excess IAA was quenched by the addition of dithiothreitol to 10 mM, followed by incubation in the dark at room temperature for 30 min. Samples were then diluted with 0.1 M ammonium bicarbonate, pH 8.0 to a final urea concentration of 2 M. Trypsin (Promega) was added at a 1:100 (enzyme: protein) ratio and digested overnight at 37°C with rotation. After digestion, 10% TFA was added to each sample to final 0.5% (pH<2). Samples were desalted under vacuum using Sep Pak C18 cartridges (Waters). Each cartridge was activated with 1 mL 80% acetonitrile (ACN)/0.1% TFA, then equilibrated three times with 1 mL of 0.1% TFA. After sample loading, cartridges were washed four times with 1 mL of 0.1% TFA, and samples were eluted four times with 0.5 mL of 50% ACN/0.25% FA. 20 µg of each sample was saved for protein abundance measurements, and the remainder was used for ubiquitylated peptides or phosphopeptides enrichment. Samples were dried by vacuum centrifugation.

For ubiquitylated peptide enrichment, 3 to 5 mg of digested and dried peptides were dissolved in 1 ml of IAP buffer (50 mM MOPS, 10 mM HNa₂PO4, 50 mM NaCl, pH 7.2) by vortexing as well as sonication, if necessary. Wash Ubiquitin Remnant Motif (K-ε-GG) Antibody Beads (CST no. 5562) twice with IAP buffer and add 10 µL of beads (resuspended in 100 µL IAP buffer) to dissolved peptides. After 2 hours incubation at 4°C with rotation, wash the beads twice with 500 µL IAP buffer (ice-

cold) by vortexing for 3x 2 s pulses and twice with 500 µL HPLC water (ice-cold). To elute K-ε-GG peptides, add 60 µL of 0.15% TFA and incubate for 10 min using Thermomixer (1500 rpm at RT). Collect the supernatant in a new tube, repeat 60 µL of 0.15% TFA addition, mix, and vortex using Thermomixer for 5 min. Add to the first elution to ensure collection of all eluted peptides. The eluted peptides were desalted using Nest C18 tips, dried, and resuspended in 15 to 20 µL of 4% FA/2% ACN before mass spectrometry.

For immobilized metal affinity chromatography (IMAC)–based phosphopeptide enrichment, 1 mg digested peptides were used. To prepare Fe-NTA beads, for each sample, 400 µL of 50% Ni-NTA Magnetic Agarose Beads (Qiagen) were transferred into Micro Bio-Spin chromatography Columns (Bio-Rad) and washed three times with 100 mM EDTA to strip nickel away and once with HPLC-grade water. To incorporate Fe, beads were resuspended in 100 mM FeCl₃, pipetted to mix, and incubated for 1 min. Excess of Fe was removed by three washes with HPLC-grade water and once with 0.5% FA. Digested peptides were resuspended in 75% ACN/0.15% TFA and incubated with the beads. After incubation, nonenriched peptides were washed out with 80% ACN/0.1% TFA. To elute phosphopeptides from beads onto Nest Tips C18 column, beads were washed twice with 500 mM potassium phosphate, pH 7.0 while pipetting to mix eight times during 2 min incubation. Potassium phosphate was removed from the Nest Tips C18 column by washing twice with 0.5% FA. In the final step, phosphopeptides were eluted from the C18 tips with 50% ACN/ 0.25% FA by spinning at 3000 rpm for 1 min and dried under vacuum centrifugation. Before MS analysis, samples were resuspended in 3% ACN/0.1% TFA.

Mass spectrometry data acquisition and analysis

For AP-MS experiments, samples were resuspended in 15 to 20 µL of MS loading buffer (1% formic acid) and 2 µL were separated by a reversed-phase gradient over a nanoflow 75µm ID x 25-cm-long picotip column packed with 1.9 µM C18 particles (Dr. Maisch). Peptides were directly injected over the course of a 75 min acquisition into a Q-Exactive Plus mass spectrometer (Thermo), or over the course of a 90 min acquisition into a Orbitrap Elite mass spectrometer. For analysis of endogenous protein abundances in parental cell lines, ~500 ng of peptides was separated over a 180 min gradient using the same column as for AP-MS experiments, and directly injected into a Q-Exactive Plus mass spectrometer. Raw MS data were searched against the UniProt canonical isoforms of the human proteome (downloaded 21 March 2018), and using the default settings in MaxQuant (version 1.6.2.10), with a match-between-runs enabled (124). Peptides and pro-

teins were filtered to 1% false discovery rate in MaxQuant, and identified proteins were then subjected to PPI scoring. To quantify changes in interactions between WT and mutant baits, or differences in endogenous protein abundances between parental cell lines, we used a label free quantification approach in which statistical analysis was performed using MSstats (125) from within the artMS R-package. All raw data files and search results are available from the Pride partner ProteomeXchange repository (126). For AP-MS and protein abundance data from MCF10A, MCF7, and MDA-MB-231 cells, these can be accessed under the PXD019639 identifier. For PTM (ub and ph) analysis data, these are available under the PXD025931 identifier.

PPI scoring

Protein spectral counts as determined by MaxQuant search results were used for PPI confidence scoring by both SAINTexpress (version 3.6.1) (25) and CompPASS (version 0.0.0.9000) (23). All PPI scoring was performed separately for each cell line. For SAINTexpress, control samples in which bait protein was not induced by doxycycline were used. For CompPASS, a stats table representing all no dox-induced samples (at least one per each bait) and WT baits was used as background control. To produce a PPI dataset of high quality, we required PPIs to pass stringent criteria by both SAINT and compPASS algorithms. In particular, the SAINTexpress scoring algorithm places a high weight on PPI reproducibility across all three replicates. Therefore, for example, candidate PPIs observed in only a single replicate would not achieve passable scores and would thus be excluded from our dataset.

When recovery rates of known PPIs (gold standard) from public databases (CORUM, BioPlex2, and BioGRID low throughput and multivalidated) (table S11) were monitored by varying thresholds of key metrics of each algorithm [Weighted D-score (WD) per bait percentile for compPASS and Bayesian false discovery rate (BFDR) for SAINTexpress, respectively], it is noticeable that CompPASS and SAINTexpress are complementary to each other, in that the best gold standard PPI recovery could be obtained when the PPIs from each algorithm are combined. Therefore, we defined a PPI score on a 0 to 1 scale, wherein WD per bait percentile and (1-BFDR) were equally weighted: PPI score = [WD per bait percentile + (1-BFDR)]/2. We filtered our PPIs with PPI score ≥ 0.9. WD score is a metric calculated from total spectral counts in compPASS (127), which incorporates the reproducibility, specificity and abundance of each interaction to aid the identification of high-confidence interacting proteins that are associated with multiple baits in a network.

Correspondence between interaction uniqueness and expression abundance analysis

For each cell line comparison, shared baits were identified. For each bait, unique preys were extracted and their corresponding global abundance log₂FC was annotated. Only preys with a detected measurement in the global abundance analysis were included. Next, the fraction of preys (unique in one cell line or another in binding to a certain bait) with a correlated (gain in interaction = increase in abundance, and vice versa) or anticorrelated (gain in interaction = decrease in abundance, and vice versa) significant change [abs(log₂FC) ≥ 1 and adjusted $P \leq 0.05$] in global abundance was calculated (fig. S1D).

Gene set enrichment analysis

Gene set enrichment analysis was performed via an overrepresentation test using the PANTHER GO Slim Biological Process database (version 14.1) (*128*). Terms with false discover rate (FDR) < 0.05 were considered. To create a network of proteins within the "DNA repair" term, the 32 enriched pathway members were used to extract a subnetwork from the STRING network (*129*). Although not differentially phosphorylated upon spinophilin KO, BRCA1 was added to the network to visualize its interconnectedness with DNA damage repair proteins.

DIS calculation

An important goal of cancer therapy is to identify drug targets that are cancer specific and are applicable across many patients. As such, we were interested in comparing PPIs across cell lines to prioritize those that were shared between cancer cell lines, but absent from the MCF10A nontumorigenic cell line. Unfortunately, a simple overlap analysis of BC PPIs identified within each cell line does not faithfully represent whether a given PPI is shared or unique in all cases. The reason for this is that to establish a finite list of BC PPIs, one must establish a threshold for such classification. This threshold strikes a balance between maximizing sensitivity for true interactions, while minimizing the inclusion of erroneous false positive interaction partners, which are often due to nonspecific binding to the beads. However, it can also be the case that real PPIs do not meet this threshold (false negatives).

To compare PPIs across cell lines, we developed a method for calculating a DIS and a corresponding FDR using AP-MS data across multiple cell lines. This approach uses the SAINTexpress score (*25*), which is the probability of a PPI being bona fide in a single cell line computed using a mixture of distribution modeling spectral counts of true and false interactions. The probabilities based on the analysis of a single cell line can then be

used to calculate a DIS between PPIs present in cancer cells and normal cells. We define a cancer-enriched DIS as the probability of the PPI being present in a cancer cell line but absent in the normal cell line. Let $S_c(p_1, p_2)$ be the SAINTexpress score of a PPI denoted as (p_1, p_2) in a cell line c. Given that PPIs are independent events across different cell lines, we compute the DIS for each (p_1, p_2) as the product of the probability of a bona fide PPI in one cell line and the probability of the PPI being false in the other cell lines, which can be denoted as follows

$$DIS_{MCF7}(p_1,p_2) = S_{MCF7}(p_1,p_2) \times (1 - S_{MDA-MB-231}(p_1,p_2)) \times (1 - S_{MCF10A}(p_1,p_2))$$

$$DIS_{MDA-MB-231}(p_1,p_2) = S_{MDA-MB-231}(p_1,p_2) \times (1 - S_{MCF7}(p_1,p_2)) \times (1 - S_{MCF10A}(p_1,p_2))$$

$$DIS_{MCF10A}(p_1,p_2) = S_{MCF10A}(p_1,p_2) \times (1 - S_{MDA-MB-231}(p_1,p_2)) \times (1 - S_{MCF7}(p_1,p_2))$$

For all DISs that we calculated, we compute the BFDR estimates at all possible thresholds $(p*)$ as follows

$$FDR(p*) = \frac{\sum_{i,i} (1 - DIS(p_i, p_j)) \times I\{DIS(p_i, p_j) > p*\}}{\sum_{i,j} I\{DIS(p_i, p_j) > p*\}}$$

where $I\{A\}$ is 1 when A is True and 0 otherwise.

Permutation test

We performed a permutation test in which genes were drawn from the list of all genes detected in the global protein abundance analysis of the parental cell lines. The null distribution of the average number of samples with variation was learned from 10,000 random gene lists of equal size to the set of interacting partners. This permutation test was performed individually for nonsynonymous mutations, CNVs, and mRNA expression. The information for observed variation of each gene is collected from the TCGA BC cohort (firehose legacy).

Assessing known interconnectedness of putative spinophilin substrates and BRCA1

Proteins with significant differential regulation of phosphorylation in spinophilin KO cells were identified by thresholding the phospho-proteomic data using $P < 0.05$ and either log₂FC > 2 or < −2. The interconnectedness of these proteins to BRCA1 (number of connections to BRCA1) was determined using either PCNet or STRING networks (black dots) and compared with 5000 random selections of equally sized sets of

proteins (blue dots) to calculate an empirical P value. When selecting the random sets of proteins, we required they be (i) detected as being phosphorylated in our phospho-proteomic analysis and (ii) not differentially phosphorylated between spinophilin WT and KO (i.e., $P > 0.05$ or abs(log₂FC) < 2). This controlled for any enrichment that could occur due to a bias toward phosphorylated proteins detected by our mass spectrometry–based approach.

IAS network

The integrated associated stringency (IAS) network was derived from integration of five major types of protein pairwise relationships recorded in public databases: (i) physical PPI; (ii) mRNA coexpression; (iii) protein coexpression; (iv) codependence (correlation of cell line growth upon gene knockouts); and (v) sequence-based relationships. A broad survey created a compendium of 127 network features used as inputs to a random forest regression model, trained to best recover the proximity of protein pairs in the Gene Ontology (GO). The final IAS score, ranging from 0 to 1, quantifies all pairwise associations among 19,035 human proteins. In this study, we displayed stringent protein interactions with IAS > 0.3 when the IAS network was used in figures. More details are described in the companion paper (*123*).

PLA

Cells were seeded in 8-well chamber slides (ibidi, 80826) at a density of 30,000 cells and 300 μL per chamber. Cells expressing transgenes of interest were dox induced 24 to 48 hours after cell seeding depending on the doubling time of the cells, at a concentration of 1 μg/mL, for ~40 hours. Cells were then harvested, with the aim of achieving between roughly 70% and 90% confluency at the time of harvest. At harvest, cells were fixed in 4% formaldehyde PBS for 15 min at room temperature. The cells were then washed in PBS and stored at 4°C until moving forward with downstream applications. Unless otherwise specified, subsequent washing steps were performed at 300μL per chamber at room temperature, and incubation steps were performed at 150 μL per chamber.

Cells were permeabilized with 0.1% Triton X-100 for 15 min at room temperature, and then washed once with PBS. Cells were blocked with the supplied 1X blocking solution in the Duolink In Situ Red Starter Kit Mouse/Rabbit (Sigma-Aldrich, DUO92101) for 60 min at 37°C. The cells were then incubated with primary antibody dilutions in the supplied Duolink Antibody Diluent (see supplementary text for primary antibody dilution ratios) at 4°C overnight.

The next day, cells were washed for 2x 5 min with the supplied Duolink Wash Buffer A. After wash, the PLA probe solution was prepared by

diluting the supplied anti-Mouse MINUS and anti-Rabbit PLUS PLA probes 1:5 in antibody diluent. The PLA probe solution was applied to the cells and allowed to incubate for 60 min at 37°C. The cells were then washed in 2x 5 min washes of wash buffer A. The Duolink Ligation Solution was then prepared by diluting the supplied 5X Ligation Buffer in high-purity water at a dilution of 1:5, and then adding to that the supplied ligase at a dilution of 1:40. The ligation solution was then applied to the cells and allowed to incubate at 37°C for 30 min. Afterward, the cells were once again washed in 2x 5 min washes of wash buffer A. The Red Duolink Amplification Solution was then prepared by diluting the supplied 5X Amplification Buffer in high-purity water at a dilution of 1:5, and then adding the supplied polymerase at a dilution of 1:80. The amplification solution was then applied to the cells and allowed to incubate for 100 min at 37°C protected from light. The final washes were then applied to the cells, consisting of 2x 10 min washes of the supplied Duolink Wash Buffer B protected from light.

The cells were then treated with a modified protocol adapted for applying a cell mask and nuclear stain to cells in multiwell plates. Cells were washed in Wash Buffer A for 2 min. Then a green cell mask (ThermoFisher, H32714) solution was prepared by diluting a 1 mg/mL starting solution 1:10,000 in Duolink Wash Buffer A. The cell mask staining solution was then applied to cells and allowed to incubate for 30 min at room temperature and protected from light. Then a Hoechst 33342 (ThermoFisher, H3570) solution was prepared by diluting the stock solution 1:1500 in Duolink Wash Buffer A. The cell mask solution was removed and then the Hoechst nuclear stain was applied directly to the cells and allowed to incubate for 10 min protected from light. The nuclear stain was then removed, and a final wash of Duolink Wash Buffer A was added to the cells. The cells were stored in Wash Buffer A at 4°C until moving forward with microscopy and imaging.

Microscopy image analysis

Samples were imaged on Nikon Ti2-E (Nikon) microscope equipped with CREST X-Light spinning disk confocal (Crest Optics), Celesta Light Engine (Lumencor), Piezo stage (Mad City Labs), Prime 95B 25 mm CMOS camera (Photometrics), and a Plan Apochromat VC 100x/1.4 Oil lens (Nikon). The red PLA dye was measured by exciting with a 561-nm laser and capturing with a 607/36 m filter. HCS CellMask Green (Invitrogen) was excited with a 488-nm laser and captured with a 511/20 filter. Nuclei/DAPI was excited with a 405-nm laser and captured with a 450/50 m filter. Z stacks were set to capture the height of all cells in the field of view and images were taken to capture > 150 cells per condition.

PLA spots in cells were segmented in 3D and counted by using GA3 analysis in NIS Elements (v. 5.30.01 build 1541, Nikon). Nuclei were segmented using the Nikon Elements machine learning segment.ai algorithm that was trained off the ground truth binaries of 4 hand segmented random Z stacks from the dataset. Adjoining nuclei were segmented further by using the separate objects module (kernel size 7x7) and nuclei were connected to 3D objects by using the connect module. Cytoplasm and divisions between the cells were determined by creating a new binary from the nuclei using the 3D erode module (by 7 pixels) and the 3D grow region and subtracting the original nuclei binaries. PLA spots were segmented through background removal by using the shading correction module with a flat field image (captured at the time of imaging), the Clarify.ai module, detecting regional maxima (count 3), and then used the denoising module. A bright spot threshold was done to isolate the puncta and puncta were separated by using the separate bright objects module. Incomplete cells that were cut off by the imaging were removed from the dataset by excluding nuclei touching the borders of the image and associated cytoplasm. The aggregate children module was used to associate nuclei and cytoplasm and to count the number of PLA spots within the 3D objects of the nuclei and cytoplasm. GA3 batch analysis in NIS Elements was used to apply the same segmentation to all images. Maximum intensity projection images were made for demonstration purposes only to show all the PLA spots in a 2D image. Images representing 3D segmentation were generated by selecting an XY slice that crossed through the center of most of the nuclei in the image and the orthogonal views for the image that were set to show as many nuclei in the image as possible.

In-cell Western blot assay and data analysis

Four independent siRNAs per target gene were purchased from Dharmacon (siGENOME SMARTpool) in Echo-compatible 384-well plates (Labcyte no. PP-0200) and resuspended in 20 µL nuclease-free water. For the assay, 4 pmol of siRNAs were aliquoted into each well of a black walled clear bottom 96-well plates (Corning no. 3904) avoiding edges using a Labcyte Echo 525. Plates were then stored at –80°C. On the day of the experiment, plates were thawed for 0.5 to 1 hour at room temperature, centrifuged at 1000 rpm for 5 min, and reconstituted with 20 µL of nuclease free water (Ambion no. AM9938) on a rotator for 30 min. Transfection reagent was prepared using 0.1% RNAiMax (Invitrogen no. 13778150) and 20% Optimem (Gibco no. 31985062) for a seeding density of 4000 cells per well; reagent was allowed to sit for 10 min at room temperature before adding 40 µL to each well and incubated for an additional

20 min. Cells grown to a confluency of 80% were lifted using 0.25% Trypsin (BioUltra no. V611X), counted, and 4000 cells were seeded per well in a 140 µL volume, resulting in 200 µL total volume for each well. Cells were incubated in a standard incubator at 37°C and 5% CO_2 for 48 hours. After the 48-hour incubation, growth media was aspirated, and cells were fixed using 50 µL per well of 4% paraformaldehyde solution (Thermo Fisher no. PI28908) for 15 min. Cells were permeabilized using 50 µL 1:100 dilution of Triton X-100 (Sigma no. 9002-93-1) in 1X PBS for 30 min, then incubated in a 2X blocking solution (2% BSA in 1X PBS) at room temperature for 2 hours. Next, blocking buffer was removed and replaced with 50 µL 1X primary antibody per well, prepared by diluting Total AKT (mouse; Cell Signaling Technologies no. 2920S) and pAKT S473 (rabbit; Cell Signaling Technologies no. 4060S) at 1:800 dilution in 1X blocking buffer (1% BSA in 1X PBS). Cells were incubated in 1X primary antibody solution overnight at 4°C. The next morning, cells were washed with 1X wash buffer (250 µL Tween-20 in 50 mL 1X PBS) and incubated for 2 hours in the dark at room temperature with 1X secondary antibody solution containing 1:1000 dilution (in 1% BSA) of anti-mouse (926-32210) and anti-rabbit (926-32211) near-infrared antibodies. Cells were washed using 1X wash buffer and resuspended in 100 µL PBS for fluorescence detection using an LiCOR Odyssey plate scanner (9140). Wavelengths for the antibodies were set to 680 nm for anti-rabbit and 800 nm for anti-mouse. To measure cell viability, PBS was aspirated, and cells were stained with 50 µL Janus Green Stain (Abcam no. ab111622) for 5 min at room temperature. Cells were washed using ultrapure water and lysed with 100 µL 0.5 m HCl shaking at 400 rpm for 10 min. A standard microplate spectrophotometer was used to measure OD 595 nm.

Raw fluorescence intensity was extracted from images using the "Trim Signal" from Image Studio Lite (LiCOR). To calculate normalized pAKT values, pAKT raw fluorescence values were first normalized to (divided by) the absorbance values for cell viability. These values were then used to calculate the median of each plate. Cell viability-normalized pAKT values were divided by these plate-specific medians before log2 transformation (pAKT only = log2[cell viability normalized pAKT / median (cell viability normalized pAKT]). Log2 fold changes for AKT were calculated similarly as for pAKT (AKT only = log2[cell viability normalized AKT / median (cell viability normalized AKT]). To calculate log2 fold change for pAKT/AKT, both pAKT and AKT raw fluorescence values were independently normalized to (divided by) their respective plate median values (median of 58 total knockdowns per plate including controls), log2 transformed,

and then subtracted (log2[normalized pAKT] – log2[normalized AKT]).

In vitro PIK3CA kinase activity assay

One hundred micrograms of recombinant PIK3CA (WT, E545K, or H1047R) and PIK3R1 complex (Promega, no. V1721, V1731, and V1741, respectively) was assembled with 1.25X PI3K reaction buffer (Promega) and 1.25X lipid substrate (PIP2:3PS, Promega no. V1701) in 20 μL reaction volume per well on 96-well plate. Recombinant BPIFA1 or SCGB2A1 (Origene no. TP313322, and no. TP309362, respectively) was twofold serially diluted in storage buffer (25 mM Tris, pH 7.4, 100 mM glycine, 10% glycerol) and 2.5 μL of each dilution was added to the PIK3CA/PIK3R1 reaction mix and incubated for 20 min at 23°C with shaking (1000 rpm) on ThermoMixer (Eppendorf). Kinase reaction was triggered by adding 2.5 μL of 250 μM ATP and further incubated for 1 hour at 23°C on ThermoMixer. To stop the enzymatic reaction and deplete uncomsumed ATP, 25 μL of ADP-Glo reagent (Promega no. V9101) with 10 mM MgCl$_2$ was added to each reaction. After incubation for 40 min at 23°C on ThermoMixer, 50 μL of kinase detection reagent (Promega no. V9101) was added to convert ADP to ATP and introduce luciferase and luciferin to detect ATP. The 96-well plate was incubated for 40 min at 23°C on ThermoMixer and the luminescence from each well was measured with SpectraMax iD3 plate reader (Molecular Devices). Each kinase reaction was performed at least in triplicate. Controls reactions (in triplicate) without enzyme or lipid substrate were included in parallel to monitor background luminescence or substrate-independent ATP hydrolysis, and these background luminescence values were subtracted from the luminescence values of actual kinase reaction.

Peptide phosphorylation assay

This assay uses a set of peptide sequences that are derived from computationally curated biological targets of kinases' substrates deposited in PhosphoAtlas (101, 130). Peptides (total 453 peptides from 237 proteins) individually allocated to separate wells in a series of 384-well plates serve as phosphorylatable probes in a large-scale ATP-consumption biochemical assay handled by automated liquid-dispensing instruments. For each experimental run, the average value of ATP concentration in sample-containing wells was used for internal normalization to calculate the phosphorylation activity per peptide as the difference in ATP consumption between each peptide-derived read out and the internal mean. For the current study, we focused on analyzing changes in peptide phosphorylation profiles measured in spinophilin KO cells compared with parental control cells. To prepare protein extracts to run on the assay platform, cells at ~85% confluency were washed

three times with cold PBS and lysed with freshly prepared 1X cell lysis buffer (1 ml per 3×10^6 cells) (10X Cell Lysis Buffer, Cell Signaling; cat. no. 9803) complemented with 1X of Halt Protease and Phosphatase (100X, ThermoScientific; cat. no. 1861281). Cell lysates were collected and spun down at 14,000 rpm for 15 min at 4°C and supernatants stored at –80°C.

Coimmunoprecipitation and Western blot analysis

Cell extracts were prepared using the same protocol as described in the Cell lysis and affinity purification section. To ensure the same amount of proteins for each sample, supernatant was quantified by Bradford protein assay prior incubation with the beads. After overnight incubation with beads at 4°C, as previously described, proteins were eluted from the beads by boiling in 2X SDS Sample Buffer (Alfa Aesar) diluted in S150 buffer and stored at –20°C.

For immunoblots, samples were loaded onto 7.5% Mini-PROTEAN TGX Precast Protein Gel (Bio-Rad). After gel electrophoresis, the samples were transferred to a membrane with Trans-Blot Turbo Transfer System (Bio-Rad). Membranes were blocked with 5% Milk TBST for 1 h at RT and incubated in the blocking solution overnight at 4°C with the indicated antibodies. The incubation was followed by washing with TBST and 1 hour incubation at RT with secondary antibodies. Bands were detected using an ECL chemiluminescence detection method with KwikQuant Ultra Digital ECL-solution, KwikQuant Imager and analyzed with KwikQuant Image Manager Software (Kindle Biosciences, LLC).

DSB GFP reporter assay

U2OS cells were reverse transfected by plating 2×10^5 cells in antibiotic-free media in a 12 well plate. Each well already contained preformed transfection complexes with 20 pmol siRNA and 3.6 μL Lipofectamine RNAiMAX Reagent (Invitrogen) in Opti-MEM used according to the manufacturer's protocol. After 20 hours, 2×10^5 cells were transferred to 6 well plates and left to recover until the next day. Transient I-SceI transfection was performed 48 hours after initial reverse transfection. About 1.92 μg I-SceI expression vector, prepared by Mini or Midi Kit (Qiagen), was used along with 24 pmol siRNA and 8.64 μL Lipofectamine 2000 Transfection Reagent (Invitrogen) in Opti-MEM according to the manufacturer's protocol. Cells were incubated with transfection complexes for 3 hours at 37°C followed by gentle washing and addition of fresh growth media with antibiotics.

Flow cytometric analysis

Approximately 72 hours after I-SceI transfection, cells were trypsinized, washed with PBS, fixed in 1% formalin and transferred to V-bottom 96-well plates. DNA repair activity

was assessed by a quantification of the percentages of GFP+ cells using the Attune NxT Flow Cytometer (ThermoFisher), and analyzed using FlowJo software (FlowJo, LLC). Experiments were performed in triplicates and error bars expressed as standard deviation (SD).

Western blot analysis

Protein extracts were performed as described previously. After Bradford analysis, we boiled samples in 1X SDS Sample Buffer and proceeded with gel electrophoresis and protein transfer onto a membrane. To detect the protein of interest, the membranes were incubated with indicated antibodies.

Cas9 RNP-mediated gene KO

crRNA:tracrRNA duplexes were formed by initially incubating 4 μl of crRNA (160 μM, Dharmacon) with 4 μl of tracrRNA (160 μM, Dharmacon) for 45 min at 37°C. Duplexes were incubated with 8 μl of Cas9-NLS protein (40 μM, MacroLab) at 37°C for 15 min. Nucleofection of Cas9 RNPs into MDA-MB-231 cells was conducted using the SE cell line 4D-nucleofector kit (Lonza, cat. no. V4SC-1960). About 200,000 cells per well were resuspended in 20 μl of supplemented SE buffer and mixed with Cas9 RNPs. Cells were nucleofected on the Amaxa 4D-Nucleofector System, using program DS-138.

After nucleofection, 80 μl of prewarmed media was added for recovery for 10 min at 37°C. For clonal selection of spinophilin KO cells, nucleofected cells were subjected to FACS sorting to seed a single cell into each well of a 96-well plate. Each clone was expanded and tested for spinophilin KO by Western blot and DNA sequencing. For Ub-proteomic analysis of polyclonal USP28 KO cells, nucleofected cells were cultured and expanded over 7 days, and depletion of USP28 protein was verified by Western blot before performing Ub-proteomic analysis.

I-SPY 2 TRIAL: Patients, data, and analysis

This correlative study involved 281 [veliparib/carboplatin (VC) arm: 71; Ctr: 210] women with high-risk stage II and III early BC who were enrolled in the multicenter, multiarm, neo-adjuvant I-SPY 2 TRIAL (NCT01042379; IND 105139) (82). Detailed descriptions of the design, eligibility, and study assessments in the I-SPY 2 trial have been reported previously, including the efficacy of investigational agents VC (81). I-SPY 2 TRIAL patients are randomized either to the control arm [paclitaxel followed by doxorubicin/cyclophosphamide; T→AC; plus trastuzumab (and later pertuzumab) if HER2+] or one of the active experimental arms. 72 HER2– patients were randomized to the VC arm from May 2010 to July 2012, and treated with veliparib and carboplatin in addition to standard taxane/anthracycline

chemotherapy (VC+T→AC) (*81*). All patients signed informed consent to allow research on and use of their biospecimen samples (*81*, *131*). Pretreatment tumor samples were assayed using Agilent 44K (*32627*) or 32K (*15746*) expression arrays; and these data were combined into a single gene-level dataset after batch-adjusting using ComBat (*132*). In our prespecified analysis plan as previously summarized (*133*, *134*), logistic regression is used to assess association with pCR in the control and experimental-arm treated populations individually. Relative biomarker performance between arms (biomarker × treatment interaction) is assessed using a logistic model (pCR~ treatment + biomarker + treatment × biomarker). Analysis is also performed adjusting for HR/HER2 (binary) status (pCR~treatment + biomarker + treatment: biomarker + HR + HER2). Markers were analyzed individually; *P* values are descriptive.

REFERENCES AND NOTES

1. R. L. Siegel, K. D. Miller, H. E. Fuchs, A. Jemal, Cancer Statistics, 2021. *CA Cancer J. Clin.* **71**, 7–33 (2021). doi: 10.3322/caac.21654; pmid: 33433946

2. Cancer Genome Atlas Network, Comprehensive molecular portraits of human breast tumours. *Nature* **490**, 61–70 (2012). doi: 10.1038/nature11412; pmid: 23000897

3. P. J. Stephens *et al.*, The landscape of cancer genes and mutational processes in breast cancer. *Nature* **486**, 400–404 (2012). doi: 10.1038/nature11017; pmid: 22722201

4. L. D. Wood *et al.*, The genomic landscapes of human breast and colorectal cancers. *Science* **318**, 1108–1113 (2007). doi: 10.1126/science.1145720; pmid: 17932254

5. A. Cho *et al.*, MUFFINN: Cancer gene discovery via network analysis of somatic mutation data. *Genome Biol.* **17**, 129 (2016). doi: 10.1186/s13059-016-0989-x; pmid: 27333808

6. T. A. Knijnenburg *et al.*, Genomic and Molecular Landscape of DNA Damage Repair Deficiency across The Cancer Genome Atlas. *Cell Rep.* **23**, 239–254.e6 (2018). doi: 10.1016/j.celrep.2018.03.076; pmid: 29617664

7. F. Sanchez-Vega *et al.*, Oncogenic Signaling Pathways in The Cancer Genome Atlas. *Cell* **173**, 321–337.e10 (2018). doi: 10.1016/j.cell.2018.03.035; pmid: 29625050

8. Mutation Consequences and Pathway Analysis Working Group of the International Cancer Genome Consortium, Pathway and network analysis of cancer genomes. *Nat. Methods* **12**, 615–621 (2015). doi: 10.1038/nmeth.3440; pmid: 26125594

9. M. Hofree, J. P. Shen, H. Carter, A. Gross, T. Ideker, Network-based stratification of tumor mutations. *Nat. Methods* **10**, 1108–1115 (2013). doi: 10.1038/nmeth.2651; pmid: 24037242

10. M. D. M. Leiserson *et al.*, Pan-cancer network analysis identifies combinations of rare somatic mutations across pathways and protein complexes. *Nat. Genet.* **47**, 106–114 (2015). doi: 10.1038/ng.3168; pmid: 25501392

11. M. Paczkowska *et al.*, Integrative pathway enrichment analysis of multivariate omics data. *Nat. Commun.* **11**, 735 (2020). doi: 10.1038/s41467-019-13983-9; pmid: 32024846

12. M. A. Reyna *et al.*, Pathway and network analysis of more than 2500 whole cancer genomes. *Nat. Commun.* **11**, 729 (2020). doi: 10.1038/s41467-020-14367-0; pmid: 32024854

13. I. W. Taylor *et al.*, Dynamic modularity in protein interaction networks predicts breast cancer outcome. *Nat. Biotechnol.* **27**, 199–204 (2009). doi: 10.1038/nbt.1522; pmid: 19182785

14. S. A. Kennedy *et al.*, Extensive rewiring of the EGFR network in colorectal cancer cells expressing transforming levels of KRAS^G13D. *Nat. Commun.* **11**, 499 (2020). doi: 10.1038/s41467-019-14224-9; pmid: 31980649

15. M. K. Gill *et al.*, A feed forward loop enforces YAP/TAZ signaling during tumorigenesis. *Nat. Commun.* **9**, 3510 (2018). doi: 10.1038/s41467-018-05939-2; pmid: 30158528

16. E. F. Harkness *et al.*, Lynch syndrome caused by MLH1 mutations is associated with an increased risk of breast cancer: A cohort study. *J. Med. Genet.* **52**, 553–556 (2015). doi: 10.1136/jmedgenet-2015-103216; pmid: 26101330

17. K. Mimori *et al.*, A single-nucleotide polymorphism of SMARCB1 in human breast cancers. *Genomics* **80**, 254–258 (2002). doi: 10.1006/geno.2002.6829; pmid: 12213194

18. W. Zheng *et al.*, Current evidences on XPC polymorphisms and breast cancer susceptibility: A meta-analysis. *Breast Cancer Res. Treat.* **128**, 811–815 (2011). doi: 10.1007/s10549-011-1369-6; pmid: 21318603

19. M. J. Hoenerhoff *et al.*, BMI1 cooperates with H-RAS to induce an aggressive breast cancer phenotype with brain metastases. *Oncogene* **28**, 3022–3032 (2009). doi: 10.1038/onc.2009.165; pmid: 19543317

20. F. Iorio *et al.*, A Landscape of Pharmacogenomic Interactions in Cancer. *Cell* **166**, 740–754 (2016). doi: 10.1016/j.cell.2016.06.017; pmid: 27397505

21. K. Yu *et al.*, Comprehensive transcriptomic analysis of cell lines as models of primary tumors across 22 tumor types. *Nat. Commun.* **10**, 3574 (2019). doi: 10.1038/s41467-019-11415-2; pmid: 31395879

22. S. Santagata *et al.*, Taxonomy of breast cancer based on normal cell phenotype predicts outcome. *J. Clin. Invest.* **124**, 859–870 (2014). doi: 10.1172/JCI70941; pmid: 24463464

23. M. E. Sowa, E. J. Bennett, S. P. Gygi, J. W. Harper, Defining the human deubiquitinating enzyme interaction landscape. *Cell* **138**, 389–403 (2009). doi: 10.1016/j.cell.2009.04.042; pmid: 19615132

24. E. L. Huttlin *et al.*, The BioPlex Network: A Systematic Exploration of the Human Interactome. *Cell* **162**, 425–440 (2015). doi: 10.1016/j.cell.2015.06.043; pmid: 26186194

25. G. Teo *et al.*, SAINTexpress: Improvements and additional features in Significance Analysis of INTeractome software. *J. Proteomics* **100**, 37–43 (2014). doi: 10.1016/j.jprot.2013.10.023; pmid: 24513533

26. E. L. Huttlin *et al.*, Architecture of the human interactome defines protein communities and disease networks. *Nature* **545**, 505–509 (2017). doi: 10.1038/nature22366; pmid: 28514442

27. E. L. Huttlin *et al.*, Dual Proteome-scale Networks Reveal Cell-specific Remodeling of the Human Interactome. *Cell* **184**, 3022–3040.e28 (2021). doi: 10.1016/j.cell.2021.04.011; pmid: 33961781

28. P. S. Shah *et al.*, Comparative Flavivirus-Host Protein Interaction Mapping Reveals Mechanisms of Dengue and Zika Virus Pathogenesis. *Cell* **175**, 1931–1945.e18 (2018). doi: 10.1016/j.cell.2018.11.028; pmid: 30550790

29. J. Batra *et al.*, Protein Interaction Mapping Identifies RBBP6 as a Negative Regulator of Ebola Virus Replication. *Cell* **175**, 1917–1930.e13 (2018). doi: 10.1016/j.cell.2018.08.044; pmid: 30550789

30. D. E. Gordon *et al.*, A SARS-CoV-2 protein interaction map reveals targets for drug repurposing. *Nature* **583**, 459–468 (2020). doi: 10.1038/s41586-020-2286-9; pmid: 32353859

31. M. Y. Hein *et al.*, A human interactome in three quantitative dimensions organized by stoichiometries and abundances. *Cell* **163**, 712–723 (2015). doi: 10.1016/j.cell.2015.09.053; pmid: 26496610

32. K. S. S. Enfield *et al.*, Epithelial tumor suppressor ELF3 is a lineage-specific amplified oncogene in lung adenocarcinoma. *Nat. Commun.* **10**, 5438 (2019). doi: 10.1038/s41467-019-13295-y; pmid: 31780666

33. M. Bouhaddou *et al.*, Mapping the protein-protein and genetic interactions of cancer to guide precision medicine. *Curr. Opin. Genet. Dev.* **54**, 110–117 (2019). doi: 10.1016/j.gde.2019.04.005; pmid: 31288129

34. M. Eckhardt *et al.*, Multiple Routes to Oncogenesis Are Promoted by the Human Papillomavirus–Host Protein Network. *Cancer Discov.* **8**, 1474–1489 (2018). doi: 10.1158/2159-8290.CD-17-1018; pmid: 30209081

35. N. del-Toro *et al.*, Capturing variation impact on molecular interactions in the IMEx Consortium mutations data set. *Nat. Commun.* **10**, 10 (2019). doi: 10.1038/s41467-018-07709-6; pmid: 30602777

36. D. L. Swaney *et al.*, A protein network map of head and neck cancer reveals PIK3CA mutant drug sensitivity. *Science* **374**, eabf2911 (2021). doi: 10.1126/science.abf2911

37. P. J. Thul *et al.*, A subcellular map of the human proteome. *Science* **356**, eaal3321 (2017). doi: 10.1126/science.aal3321; pmid: 28495876

38. E. Grabocka *et al.*, Wild-type H- and N-Ras promote mutant K-Ras-driven tumorigenesis by modulating the DNA damage response. *Cancer Cell* **25**, 243–256 (2014). doi: 10.1016/j.ccr.2014.01.005; pmid: 24525237

39. C. Forcet *et al.*, Functional analysis of Peutz-Jeghers mutations reveals that the LKB1 C-terminal region exerts a crucial role in regulating both the AMPK pathway and the cell polarity. *Hum. Mol. Genet.* **14**, 1283–1292 (2005). doi: 10.1093/hmg/ddi139; pmid: 15800014

40. X. Xu, T. Omelchenko, A. Hall, LKB1 tumor suppressor protein regulates actin filament assembly through Rho and its exchange factor Dbl independently of kinase activity. *BMC Cell Biol.* **11**, 77 (2010). doi: 10.1186/1471-2121-11-77; pmid: 20939895

41. W. M. Brieher, A. S. Yap, Cadherin junctions and their cytoskeleton(s). *Curr. Opin. Cell Biol.* **25**, 39–46 (2013). doi: 10.1016/j.ceb.2012.10.010; pmid: 23127608

42. M. Canel, A. Serrels, M. C. Frame, V. G. Brunton, E-cadherin–integrin crosstalk in cancer invasion and metastasis. *J. Cell Sci.* **126**, 393–401 (2013). doi: 10.1242/jcs.100115; pmid: 23525005

43. M. Lombaerts *et al.*, E-cadherin transcriptional downregulation by promoter methylation but not mutation is related to epithelial-to-mesenchymal transition in breast cancer cell lines. *Br. J. Cancer* **94**, 661–671 (2006). doi: 10.1038/sj.bjc.6602996; pmid: 16495925

44. E. Zeqiraj *et al.*, ATP and MO25α regulate the conformational state of the STRADα pseudokinase and activation of the LKB1 tumour suppressor. *PLOS Biol.* **7**, e1000126 (2009). doi: 10.1371/journal.pbio.1000126; pmid: 19513107

45. E. Zeqiraj, B. M. Filippi, M. Deak, D. R. Alessi, D. M. F. van Aalten, Structure of the LKB1-STRAD-MO25 complex reveals an allosteric mechanism of kinase activation. *Science* **326**, 1707–1711 (2009). doi: 10.1126/science.1178377; pmid: 19892943

46. D. G. Hardie, D. R. Alessi, LKB1 and AMPK and the cancer-metabolism link - ten years after. *BMC Biol.* **11**, 36 (2013). doi: 10.1186/1741-7007-11-36; pmid: 23587167

47. P. E. Hollstein *et al.*, The AMPK-Related Kinases SIK1 and SIK3 Mediate Key Tumor-Suppressive Effects of LKB1 in NSCLC. *Cancer Discov.* **9**, 1606–1627 (2019). doi: 10.1158/2159-8290.CD-18-1261; pmid: 31350328

48. J. M. Lizcano *et al.*, LKB1 is a master kinase that activates 13 kinases of the AMPK subfamily, including MARK/PAR-1. *EMBO J.* **23**, 833–843 (2004). doi: 10.1038/sj.emboj.7600110; pmid: 14976552

49. S.-W. Lee *et al.*, Skp2-dependent ubiquitination and activation of LKB1 is essential for cancer cell survival under energy stress. *Mol. Cell* **57**, 1022–1033 (2015). doi: 10.1016/j.molcel.2015.01.015; pmid: 25728766

50. J. D. Carpten *et al.*, A transforming mutation in the pleckstrin homology domain of AKT1 in cancer. *Nature* **448**, 439–444 (2007). doi: 10.1038/nature05933; pmid: 17611497

51. I. Vivanco, C. L. Sawyers, The phosphatidylinositol 3-Kinase AKT pathway in human cancer. *Nat. Rev. Cancer* **2**, 489–501 (2002). doi: 10.1038/nrc839; pmid: 12094235

52. D. A. Fruman *et al.*, The PI3K Pathway in Human Disease. *Cell* **170**, 605–635 (2017). doi: 10.1016/j.cell.2017.07.029; pmid: 28802037

53. T. A. Yap *et al.*, First-in-man clinical trial of the oral pan-AKT inhibitor MK-2206 in patients with advanced solid tumors. *J. Clin. Oncol.* **29**, 4688–4695 (2011). doi: 10.1200/JCO.2011.35.5263; pmid: 22025163

54. D. R. Alessi *et al.*, Characterization of a 3-phosphoinositide-dependent protein kinase which phosphorylates and activates protein kinase Bα. *Curr. Biol.* **7**, 261–269 (1997). doi: 10.1016/S0960-9822(06)00122-9; pmid: 9094314

55. D. Stokoe *et al.*, Dual role of phosphatidylinositol-3,4,5-trisphosphate in the activation of protein kinase B. *Science* **277**, 567–570 (1997). doi: 10.1126/science.277.5325.567; pmid: 9228007

56. A. Tzatsos, K. V. Kandror, Nutrients suppress phosphatidylinositol 3-kinase/Akt signaling via raptor-dependent mTOR-mediated insulin receptor substrate 1 phosphorylation. *Mol. Cell. Biol.* **26**, 63–76 (2006). doi: 10.1128/MCB.26.1.63-76.2006; pmid: 16354680

57. R. Woscholski, R. Dhand, M. J. Fry, M. D. Waterfield, P. J. Parker, Biochemical characterization of the free catalytic p110α and the complexed heterodimeric p110α.p85α forms of the mammalian phosphatidylinositol 3-kinase. *J. Biol. Chem.* **269**, 25067–25072 (1994). doi: 10.1016/S0021-9258(17)31499-0; pmid: 7929193

58. S. Kuchay *et al.*, FBXL2- and PTPL1-mediated degradation of p110-free p85β regulatory subunit controls the PI(3)K signalling cascade. *Nat. Cell Biol.* **15**, 472–480 (2013). doi: 10.1038/ncb2731; pmid: 23604317

59. I. Mothe *et al.*, Interaction of wild type and dominant-negative p55PIK regulatory subunit of phosphatidylinositol 3-kinase with insulin-like growth factor-1 signaling proteins.

Mol. Endocrinol. **11**, 1911–1923 (1997). doi: 10.1210/mend.11.13.0029; pmid: 9415396

60. H. Chen *et al.*, A cell-based immunocytochemical assay for monitoring kinase signaling pathways and drug efficacy. *Anal. Biochem.* **338**, 136–142 (2005). doi: 10.1016/j.ab.2004.11.015; pmid: 15707944

61. L. C. Cantley, B. G. Neel, New insights into tumor suppression: PTEN suppresses tumor formation by restraining the phosphoinositide 3-kinase/AKT pathway. *Proc. Natl. Acad. Sci. U.S.A.* **96**, 4240–4245 (1999). doi: 10.1073/pnas.96.8.4240; pmid: 10200246

62. P. A. Futreal *et al.*, BRCA1 mutations in primary breast and ovarian carcinomas. *Science* **266**, 120–122 (1994). doi: 10.1126/science.7939630; pmid: 7939630

63. Y. Miki *et al.*, A strong candidate for the breast and ovarian cancer susceptibility gene BRCA1. *Science* **266**, 66–71 (1994). doi: 10.1126/science.7545954; pmid: 7545954

64. R. Prakash, Y. Zhang, W. Feng, M. Jasin, Homologous recombination and human health: The roles of BRCA1, BRCA2, and associated proteins. *Cold Spring Harb. Perspect. Biol.* **7**, a016600 (2015). doi: 10.1101/cshperspect.a016600; pmid: 25833843

65. P. B. Mullan, J. E. Quinn, D. P. Harkin, The role of BRCA1 in transcriptional regulation and cell cycle control. *Oncogene* **25**, 5854–5863 (2006). doi: 10.1038/sj.onc.1209872; pmid: 16998500

66. S. J. Hill *et al.*, Systematic screening reveals a role for BRCA1 in the response to transcription-associated DNA damage. *Genes Dev.* **28**, 1957–1975 (2014). doi: 10.1101/gad.241620.114; pmid: 25184681

67. L. C. Wu *et al.*, Identification of a RING protein that can interact in vivo with the BRCA1 gene product. *Nat. Genet.* **14**, 430–440 (1996). doi: 10.1038/ng1296-430; pmid: 8944023

68. X. Yu, C. C. Chini, M. He, G. Mer, J. Chen, The BRCT domain is a phospho-protein binding domain. *Science* **302**, 639–642 (2003). doi: 10.1126/science.1088753; pmid: 14576433

69. B. Górski *et al.*, Founder mutations in the BRCA1 gene in Polish families with breast-ovarian cancer. *Am. J. Hum. Genet.* **66**, 1963–1968 (2000). doi: 10.1086/302922; pmid: 10788334

70. A. Vega *et al.*, The R71G BRCA1 is a founder Spanish mutation and leads to aberrant splicing of the transcript. *Hum. Mutat.* **17**, 520–521 (2001). doi: 10.1002/humu.1136; pmid: 11385711

71. E. Levy-Lahad *et al.*, Founder BRCA1 and BRCA2 mutations in Ashkenazi Jews in Israel: Frequency and differential penetrance in ovarian cancer and in breast-ovarian cancer families. *Am. J. Hum. Genet.* **60**, 1059–1067 (1997). pmid: 9150153

72. J. A. Clapperton *et al.*, Structure and mechanism of BRCA1 BRCT domain recognition of phosphorylated BACH1 with implications for cancer. *Nat. Struct. Mol. Biol.* **11**, 512–518 (2004). doi: 10.1038/nsmb775; pmid: 15133502

73. Y. Wang *et al.*, The BRCA1-Δ11q Alternative Splice Isoform Bypasses Germline Mutations and Promotes Therapeutic Resistance to PARP Inhibition and Cisplatin. *Cancer Res.* **76**, 2778–2790 (2016). doi: 10.1158/0008-5472.CAN-16-0186; pmid: 27197267

74. R. Shakya *et al.*, BRCA1 tumor suppression depends on BRCT phosphoprotein binding, but not its E3 ligase activity. *Science* **334**, 525–528 (2011). doi: 10.1126/science.1209909; pmid: 22034435

75. H. Holstege *et al.*, High incidence of protein-truncating TP53 mutations in BRCA1-related breast cancer. *Cancer Res.* **69**, 3625–3633 (2009). doi: 10.1158/0008-5472.CAN-08-3426; pmid: 19336573

76. X. Yu, J. Chen, DNA damage-induced cell cycle checkpoint control requires CtIP, a phosphorylation-dependent binding partner of BRCA1 C-terminal domains. *Mol. Cell. Biol.* **24**, 9478–9486 (2004). doi: 10.1128/MCB.24.21.9478-9486.2004; pmid: 15485915

77. Y. Wang *et al.*, RING domain-deficient BRCA1 promotes PARP inhibitor and platinum resistance. *J. Clin. Invest.* **126**, 3145–3157 (2016). doi: 10.1172/JCI87033; pmid: 27454289

78. R. Drost *et al.*, BRCA1185delAG tumors may acquire therapy resistance through expression of RING-less BRCA1. *J. Clin. Invest.* **126**, 2903–2918 (2016). doi: 10.1172/JCI70196; pmid: 27454287

79. D. E. Christensen, P. S. Brzovic, R. E. Klevit, E2-BRCA1 RING interactions dictate synthesis of mono- or specific polyubiquitin chain linkages. *Nat. Struct. Mol. Biol.* **14**, 941–948 (2007). doi: 10.1038/nsmb1295; pmid: 17873885

80. G. Y. Zhao *et al.*, A critical role for the ubiquitin-conjugating enzyme Ubc13 in initiating homologous recombination. *Mol. Cell* **25**, 663–675 (2007). doi: 10.1016/j.molcel.2007.01.029; pmid: 17349954

81. H. S. Rugo *et al.*, Adaptive Randomization of Veliparib–Carboplatin Treatment in Breast Cancer. *N. Engl. J. Med.* **375**, 23–34 (2016). doi: 10.1056/NEJMoa1513749; pmid: 27406347

82. A. D. Barker *et al.*, I-SPY 2: An adaptive breast cancer trial design in the setting of neoadjuvant chemotherapy. *Clin. Pharmacol. Ther.* **86**, 97–100 (2009). doi: 10.1038/clpt.2009.68; pmid: 19440188

83. M. Zimmermann *et al.*, CRISPR screens identify genomic ribonucleotides as a source of PARP-trapping lesions. *Nature* **559**, 285–289 (2018). doi: 10.1038/s41586-018-0291-z; pmid: 29973717

84. D. Zhang, K. Zaugg, T. W. Mak, S. J. Elledge, A role for the deubiquitinating enzyme USP28 in control of the DNA-damage response. *Cell* **126**, 529–542 (2006). doi: 10.1016/j.cell.2006.06.039; pmid: 16901786

85. F. Bassermann *et al.*, The Cdc14B-Cdh1-Plk1 axis controls the G2 DNA-damage-response checkpoint. *Cell* **134**, 256–267 (2008). doi: 10.1016/j.cell.2008.05.043; pmid: 18662541

86. P. A. Knobel *et al.*, USP28 is recruited to sites of DNA damage by the tandem BRCT domains of 53BP1 but plays a minor role in double-strand break metabolism. *Mol. Cell. Biol.* **34**, 2062–2074 (2014). doi: 10.1128/MCB.00197-14; pmid: 24687851

87. A. Gunn, J. M. Stark, I-SceI-based assays to examine distinct repair outcomes of mammalian chromosomal double strand breaks. *Methods Mol. Biol.* **920**, 379–391 (2012). doi: 10.1007/978-1-61779-998-3_27; pmid: 22941618

88. R. W. Anantha *et al.*, Functional and mutational landscapes of BRCA1 for homology-directed repair and therapy resistance. *eLife* **6**, e21350 (2017). doi: 10.7554/eLife.21350; pmid: 28398198

89. J. F. Hultquist *et al.*, CRISPR-Cas9 genome engineering of primary CD4$^+$ T cells for the interrogation of HIV-host factor interactions. *Nat. Protoc.* **14**, 1–27 (2019). doi: 10.1038/s41596-018-0069-7; pmid: 30559373

90. P. Moudry *et al.*, Ubiquitin-activating enzyme UBA1 is required for cellular response to DNA damage. *Cell Cycle* **11**, 1573–1582 (2012). doi: 10.4161/cc.19978; pmid: 22456334

91. I. Unk *et al.*, Human SHPRH is a ubiquitin ligase for Mms2-Ubc13-dependent polyubiquitylation of proliferating cell nuclear antigen. *Proc. Natl. Acad. Sci. U.S.A.* **103**, 18107–18112 (2006). doi: 10.1073/pnas.0608595103; pmid: 17108083

92. H. Wang *et al.*, Histone H3 and H4 ubiquitylation by the CUL4-DDB-ROC1 ubiquitin ligase facilitates cellular response to DNA damage. *Mol. Cell* **22**, 383–394 (2006). doi: 10.1016/j.molcel.2006.03.035; pmid: 16678110

93. Y. Chen, C. Weng, H. Zhang, J. Sun, Y. Yuan, A Direct Interaction Between P53-Binding Protein 1 and Minichromosome Maintenance Complex in Hepg2 Cells. *Cell. Physiol. Biochem.* **47**, 2350–2359 (2018). doi: 10.1159/000491607; pmid: 29990989

94. D. Sarrouilhe, A. di Tommaso, T. Métayé, V. Ladeveze, Spinophilin: From partners to functions. *Biochimie* **88**, 1099–1113 (2006). doi: 10.1016/j.biochi.2006.04.010; pmid: 16737766

95. N. T. Woods *et al.*, Charting the landscape of tandem BRCT domain-mediated protein interactions. *Sci. Signal.* **5**, rs6 (2012). doi: 10.1126/scisignal.2002255; pmid: 22990118

96. Q. Wu, H. Jubb, T. L. Blundell, Phosphopeptide interactions with BRCA1 BRCT domains: More than just a motif. *Prog. Biophys. Mol. Biol.* **117**, 143–148 (2015). doi: 10.1016/j.pbiomolbio.2015.02.003; pmid: 25701377

97. Q. Wu *et al.*, Structure of BRCA1-BRCT/Abraxas Complex Reveals Phosphorylation-Dependent BRCT Dimerization at DNA Damage Sites. *Mol. Cell* **61**, 434–448 (2016). doi: 10.1016/j.molcel.2015.12.017; pmid: 26778126

98. M. J. Ragusa *et al.*, Spinophilin directs protein phosphatase 1 specificity by blocking substrate binding sites. *Nat. Struct. Mol. Biol.* **17**, 459–464 (2010). doi: 10.1038/nsmb.1786; pmid: 20305656

99. L. M. Sack *et al.*, Profound Tissue Specificity in Proliferation Control Underlies Cancer Drivers and Aneuploidy Patterns. *Cell* **173**, 499–514.e23 (2018). doi: 10.1016/j.cell.2018.02.037; pmid: 29576454

100. J. P. Coppé *et al.*, Mapping phospho-catalytic dependencies of therapy-resistant tumours reveals actionable

vulnerabilities. *Nat. Cell Biol.* **21**, 778–790 (2019). doi: 10.1038/s41556-019-0328-z; pmid: 31160710

101. A. Olow *et al.*, An Atlas of the Human Kinome Reveals the Mutational Landscape Underlying Dysregulated Phosphorylation Cascades in Cancer. *Cancer Res.* **76**, 1733–1745 (2016). doi: 10.1158/0008-5472.CAN-15-2325-T; pmid: 26921330

102. C. V. Hinton, L. D. Fitzgerald, M. E. Thompson, Phosphatidylinositol 3-kinase/Akt signaling enhances nuclear localization and transcriptional activity of BRCA1. *Exp. Cell Res.* **313**, 1735–1744 (2007). doi: 10.1016/j.yexcr.2007.03.008; pmid: 17428466

103. J. M. Beckta *et al.*, Mutation of the BRCA1 SQ-cluster results in aberrant mitosis, reduced homologous recombination, and a compensatory increase in non-homologous end joining. *Oncotarget* **6**, 27674–27687 (2015). doi: 10.18632/oncotarget.4876; pmid: 26320175

104. B. Xu, A. H. O'Donnell, S.-T. Kim, M. B. Kastan, Phosphorylation of serine 1387 in Brca1 is specifically required for the Atm-mediated S-phase checkpoint after ionizing irradiation. *Cancer Res.* **62**, 4588–4591 (2002). pmid: 12183412

105. D. Cortez, Y. Wang, J. Qin, S. J. Elledge, Requirement of ATM-dependent phosphorylation of brca1 in the DNA damage response to double-strand breaks. *Science* **286**, 1162–1166 (1999). doi: 10.1126/science.286.5442.1162; pmid: 10550055

106. E. P. Rogakou, D. R. Pilch, A. H. Orr, V. S. Ivanova, W. M. Bonner, DNA double-stranded breaks induce histone H2AX phosphorylation on serine 139. *J. Biol. Chem.* **273**, 5858–5868 (1998). doi: 10.1074/jbc.273.10.5858; pmid: 9488723

107. J. Lukas, C. Lukas, J. Bartek, More than just a focus: The chromatin response to DNA damage and its role in genome integrity maintenance. *Nat. Cell Biol.* **13**, 1161–1169 (2011). doi: 10.1038/ncb2344; pmid: 21968989

108. B. Alberts, The cell as a collection of protein machines: Preparing the next generation of molecular biologists. *Cell* **92**, 291–294 (1998). doi: 10.1016/S0092-8674(00)80922-8; pmid: 9476889

109. D. Hanahan, R. A. Weinberg, The hallmarks of cancer. *Cell* **100**, 57–70 (2000). doi: 10.1016/S0092-8674(00)81683-9; pmid: 10647931

110. N. J. Krogan, S. Lippman, D. A. Agard, A. Ashworth, T. Ideker, The cancer cell map initiative: Defining the hallmark networks of cancer. *Mol. Cell* **58**, 690–698 (2015). doi: 10.1016/j.molcel.2015.05.008; pmid: 26000852

111. K. C. Goldfarbmuren *et al.*, Dissecting the cellular specificity of smoking effects and reconstructing lineages in the human airway epithelium. *Nat. Commun.* **11**, 2485 (2020). doi: 10.1038/s41467-020-16239-z; pmid: 32427931

112. C. J. Britto, L. Cohn, Bactericidal/Permeability-increasing protein fold-containing family member A1 in airway host protection and respiratory disease. *Am. J. Respir. Cell Mol. Biol.* **52**, 525–534 (2015). doi: 10.1165/rcmb.2014-0297RT; pmid: 25265466

113. L. Bingle, C. D. Bingle, Distribution of human PLUNC/BPI fold-containing (BPIF) proteins. *Biochem. Soc. Trans.* **39**, 1023–1027 (2011). doi: 10.1042/BST0391023; pmid: 21787341

114. Y. He *et al.*, Association of PLUNC gene polymorphisms with susceptibility to nasopharyngeal carcinoma in a Chinese population. *J. Med. Genet.* **42**, 172–176 (2005). doi: 10.1136/jmg.2004.022616; pmid: 15689457

115. P. Chen *et al.*, SPLUNC1 regulates cell progression and apoptosis through the miR-141-PTEN/p27 pathway, but is hindered by LMP1. *PLOS ONE* **8**, e56929 (2013). doi: 10.1371/journal.pone.0056929; pmid: 23472073

116. T. Aihara *et al.*, Mammaglobin B as a novel marker for detection of breast cancer micrometastases in axillary lymph nodes by reverse transcription-polymerase chain reaction. *Breast Cancer Res. Treat.* **58**, 137–140 (1999). doi: 10.1023/A:1006335817889; pmid: 10674878

117. R. A. Tassi *et al.*, Mammaglobin B expression in human endometrial cancer. *Int. J. Gynecol. Cancer* **18**, 1090–1096 (2008). doi: 10.1111/j.1525-1438.2007.01137.x; pmid: 18021217

118. P. Zubor *et al.*, Gene expression abnormalities in histologically normal breast epithelium from patients with luminal type of breast cancer. *Mol. Biol. Rep.* **42**, 977–988 (2015). doi: 10.1007/s11033-014-3834-x; pmid: 25407308

119. H. Zhou *et al.*, Decreased secretoglobin family 2A member 1expression is associated with poor outcomes in endometrial

cancer. *Oncol. Lett.* **20**, 24 (2020). doi: 10.3892/ol.2020.11885; pmid: 32774497

120. S. Park, F. Supek, B. Lehner, Systematic discovery of germline cancer predisposition genes through the identification of somatic second hits. *Nat. Commun.* **9**, 2601 (2018). doi: 10.1038/s41467-018-04900-7; pmid: 29973584

121. M. Quanz *et al.*, Hyperactivation of DNA-PK by double-strand break mimicking molecules disorganizes DNA damage response. *PLOS ONE* **4**, e6298 (2009). doi: 10.1371/journal.pone.0006298; pmid: 19621083

122. A. Bensimon *et al.*, ATM-dependent and -independent dynamics of the nuclear phosphoproteome after DNA damage. *Sci. Signal.* **3**, rs3 (2010). doi: 10.1126/scisignal.2001034; pmid: 21139141

123. F. Zheng *et al.*, Interpretation of cancer mutations using a multiscale map of protein systems. *Science* **374**, eabf3067 (2021). doi: 10.1126/science.abf3067

124. J. Cox, M. Mann, MaxQuant enables high peptide identification rates, individualized p.p.b.-range mass accuracies and proteome-wide protein quantification. *Nat. Biotechnol.* **26**, 1367–1372 (2008). doi: 10.1038/nbt.1511; pmid: 19029910

125. M. Choi *et al.*, MSstats: An R package for statistical analysis of quantitative mass spectrometry-based proteomic experiments. *Bioinformatics* **30**, 2524–2526 (2014). doi: 10.1093/bioinformatics/btu305; pmid: 24794931

126. J. A. Vizcaíno *et al.*, ProteomeXchange provides globally coordinated proteomics data submission and dissemination. *Nat. Biotechnol.* **32**, 223–226 (2014). doi: 10.1038/nbt.2839; pmid: 24727771

127. C. Behrends, M. E. Sowa, S. P. Gygi, J. W. Harper, Network organization of the human autophagy system. *Nature* **466**, 68–76 (2010). doi: 10.1038/nature09204; pmid: 20562859

128. H. Mi *et al.*, PANTHER version 16: A revised family classification, tree-based classification tool, enhancer regions and extensive API. *Nucleic Acids Res.* **49**, D394–D403 (2021). doi: 10.1093/nar/gkaa1106; pmid: 33290554

129. D. Szklarczyk *et al.*, The STRING database in 2017: Quality-controlled protein-protein association networks, made broadly accessible. *Nucleic Acids Res.* **45**, D362–D368 (2017). doi: 10.1093/nar/gkw937; pmid: 27924014

130. Z. Chen, J.-P. Coppé, Method and System for Building and Using a Centralized and Harmonized Relational Database, US Patent US 2012/0296880 A1 (2012).

131. A. J. Chien *et al.*, MK-2206 and Standard Neoadjuvant Chemotherapy Improves Response in Patients With Human Epidermal Growth Factor Receptor 2-Positive and/or Hormone Receptor-Negative Breast Cancers in the I-SPY 2 Trial. *J. Clin. Oncol.* **38**, 1059–1069 (2020). doi: 10.1200/JCO.19.01027; pmid: 32031889

132. W. E. Johnson, C. Li, A. Rabinovic, Adjusting batch effects in microarray expression data using empirical Bayes methods. *Biostatistics* **8**, 118–127 (2007). doi: 10.1093/biostatistics/kxj037; pmid: 16632515

133. J. D. Wulfkuhle *et al.*, Evaluation of the HER/PI3K/AKT Family Signaling Network as a Predictive Biomarker of Pathologic Complete Response for Patients With Breast Cancer Treated With Neratinib in the I-SPY 2 TRIAL. *JCO Precis. Oncol.* **2018**, 1–20 (2018). doi: 10.1200/PO.18.00024

134. D. M. Wolf *et al.*, DNA repair deficiency biomarkers and the 70-gene ultra-high risk signature as predictors of veliparib/carboplatin response in the I-SPY 2 breast cancer trial. *NPJ Breast Cancer* **3**, 31 (2017). doi: 10.1038/s41523-017-0025-7; pmid: 28948212

Science

A protein interaction landscape of breast cancer

Minkyu KimJisoo ParkMehdi BouhaddouKyumin KimAjda RojcMaya ModakMargaret SoucherayMichael J. McGregorPatrick O'LearyDenise WolfErica StevensonTzeh Keong FooDominique MitchellKari A. HerringtonDenise P. MuñozBeril TutuncuogluKuei-Ho ChenFan ZhengJason F. KreisbergMorgan E. DiolaitiJohn D. GordanJean-Philippe CoppéDanielle L. SwaneyBing XiaLaura van 't VeerAlan AshworthTrey IdekerNevan J. Krogan

Mapping protein interactions driving cancer

Cancer is a genetic disease, and much cancer research is focused on identifying carcinogenic mutations and determining how they relate to disease progression. Three papers demonstrate how mutations are processed through networks of protein interactions to promote cancer (see the Perspective by Cheng and Jackson). Swaney *et al.* focus on head and neck cancer and identify cancer-enriched interactions, demonstrating how point mutant–dependent interactions of PIK3CA, a kinase frequently mutated in human cancers, are predictive of drug response. Kim *et al.* focus on breast cancer and identify two proteins functionally connected to the tumor-suppressor gene BRCA1 and two proteins that regulate PIK3CA. Zheng *et al.* developed a statistical model that identifies protein networks that are under mutation pressure across different cancer types, including a complex bringing together PIK3CA with actomyosin proteins. These papers provide a resource that will be helpful in interpreting cancer genomic data. —VV

View the article online
https://www.science.org/doi/10.1126/science.abf3066
Permissions
https://www.science.org/help/reprints-and-permissions

Use of think article is subject to the Terms of service